Key Points:
- Vertically resolved weak temperature gradient analysis suggests MJO is strongly supported by radiative feedbacks and damped by horizontal advection
- Changes in the vertical structure of apparent heating do not play a dominant role in limiting the amplitude of the MJO in SP-CESM
- Process oriented diagnostics are needed to assess if "correct" combination of processes are driving moisture-convection feedbacks in models

Correspondence to:
B. O. Wolding,
Brandon.Wolding@gmail.com

Vertically resolved weak temperature gradient analysis of the Madden-Julian Oscillation in SP-CESM

Brandon O. Wolding[1], Eric D. Maloney[1], and Mark Branson[1]

[1]Department of Atmospheric Science, Colorado State University, Fort Collins, Colorado, USA

Abstract The collective effects of convection can influence large-scale circulations that, in turn, act to organize convective activity. Such scale interactions may play an important role in moisture-convection feedbacks thought to be important to both convective aggregation and the Madden-Julian Oscillation, yet such interactions are not fully understood. New diagnostics based on tropical weak temperature gradient (WTG) theory have begun to make this problem more tractable, and are leveraged in this study to analyze the relationship between various apparent heating processes and large-scale vertical moisture advection in SP-CESM. WTG theory provides a framework for accurately diagnosing intraseasonal variations in large-scale vertical motion from apparent heating, allowing large-scale vertical moisture advection to be decomposed into contributions from microphysical processes, subgrid scale eddy fluxes, and radiative heating. This approach is consistent with the column moist static energy (MSE) budget approach, and has the added benefit of allowing the vertical advection term of the column MSE budget to be quantitatively partitioned into contributions from the aforementioned apparent heating processes. This decomposition is used to show that the MJO is an instability strongly supported by radiative feedbacks and damped by horizontal advection, consistent with the findings of previous studies. Periods of low, moderate, and high MJO amplitude are compared, and it is shown that changes in the vertical structure of apparent heating do not play a dominant role in limiting the amplitude of the MJO in SP-CESM. Finally, a diagnostic approach to scale analysis of tropical dynamics is used to investigate how the governing dynamics of various phenomena differ throughout wavenumber-frequency space. Findings support previous studies that suggest the governing dynamics of the MJO differ from those of strongly divergent convectively coupled equatorial waves.

1. Introduction

The organization of clouds spans a wide range of spatial and temporal scales, from phenomena directly observable by individuals within a few hours or less, to those observable only given the perspective provided by modern satellites. Such organization not only manifests itself through variations in weather, but also influences fundamental features of our climate, including the Earth's energy balance, and remains a substantial source of uncertainty in projections of future climate [*Stocker et al.*, 2014; *Bony et al.*, 2015]. Large-scale circulations often play an important role in driving the organization of clouds. In turn, the aggregate effect of individual clouds and cloud systems, which broker radiative transfer and redistribute heat, moisture, and momentum, can influence large-scale circulations. This scale interaction provides the potential for feedbacks to develop between clouds and large-scale circulations.

Convective aggregation, a special form of organization that may potentially be driven by such a feedback, has been documented in cloud-system-resolving-model (CSRM) simulations in radiative-convective equilibrium [*Bretherton et al.*, 2005; *Wing and Emanuel*, 2014] and, more recently, in near global [*Bretherton and Khairoutdinov*, 2015] and global scale [*Arnold and Randall*, 2015] aquaplanet simulations. Under certain conditions, these simulations exhibit the rapid development of dry regions that expand until convection, initially randomly distributed, had self-aggregated into isolated regions. When Earth-like rotation was included in the simulation of *Arnold and Randall* [2015], the model produced a robust Madden-Julian Oscillation (MJO) that appeared to be destabilized by processes similar to those driving convective aggregation in the nonrotating simulations. Such findings suggest that the processes responsible for convective aggregation in these idealized studies may also play a fundamental role in the real world MJO. Understanding these processes has been posed as one of the "grand challenges" [*Bony et al.*, 2015] to atmospheric science, not only

because of their importance for understanding the MJO, but also because of their potential role in climate sensitivity and feedbacks.

Interactions between moisture and convection, both at the convective scale and the large-scale, appear to play a fundamental role in both the MJO and convective aggregation. At the convective-scale, the large lower tropospheric entrainment that occurs in tropical oceanic convection [*Lucas et al.*, 1994; *Zipser*, 2003] allows free tropospheric moisture content to modulate convective activity. Convection can redistribute moisture locally, conditioning the environment in ways that can favor or suppress subsequent convection [*Tompkins*, 2001]. At the large-scale, the aggregate effect of a convective population can modify large-scale circulations that, in turn, affect the large-scale moisture content. If regions of enhanced or suppressed convection impact large-scale circulations in such a way that further moistening or drying of those regions occurs respectively, a modal instability, as proposed by moisture mode theory [*Sobel et al.*, 2001; *Raymond*, 2001], may occur [*Fuchs and Raymond*, 2005; *Raymond and Fuchs*, 2009; *Sobel and Maloney*, 2012; *Arnold and Randall*, 2015; *Adames and Kim*, 2016]. Increasing column moisture variance and a progressively more bi-modal distribution of column water vapor may signal the development of such an instability, and are observed in simulations of convective aggregation as well as during periods of enhanced MJO activity. Understanding the processes that act to increase column moisture variance (i.e., promote the development of anomalously moist and dry patches) is an important component of understanding the processes responsible for such modal instability.

Budgets analyses of column moist static energy (MSE) and column MSE variance, commonly used in studies of both the MJO [*Maloney*, 2009; *Kiranmayi and Maloney*, 2011; *Andersen and Kuang*, 2012; *Wu and Deng*, 2013; *Kim et al.*, 2014a; *Sobel et al.*, 2014; *Arnold et al.*, 2015; *Wolding and Maloney*, 2015a] and convective aggregation [*Bretherton et al.*, 2005; *Wing and Emanuel*, 2014; *Bretherton and Khairoutdinov*, 2015; *Arnold and Randall*, 2015; *Muller and Bony*, 2015], have provided great insight to the processes controlling column moisture and column moisture variance. Budget analyses of changes in column MSE, which closely reflect changes in column moisture under weak temperature gradient (WTG) balance, have the desirable attribute of accounting for the coupled nature of apparent heating and moisture convergence driven by that heating, thereby allowing the effect of radiative heating on column moisture to be estimated. While the MJO differs from the convective aggregation produced in modeling studies in important ways, most notably the larger zonal scale and zonal asymmetry of the former, the aforementioned MSE analyses highlight fundamental similarities between these phenomena. These studies generally agree that, when established, both forms of instability are maintained by diabatic feedbacks that transfer MSE up gradient, and that longwave radiative feedbacks play a critical role in this transfer. General agreement also exists that horizontal advection plays an important role in limiting the further growth of these instabilities once they are established. The role of surface flux feedbacks remains less clear, appearing to play a destabilizing role in observational studies of the MJO [*Kiranmayi and Maloney*, 2011; *Kim et al.*, 2014a; *Sobel et al.*, 2014; *Wolding and Maloney*, 2015a; *Riley Dellaripa and Maloney*, 2015] and being necessary for aggregation in some RCE simulations [*Bretherton et al.*, 2005], while acting to stabilize the MJO in some model simulations [*Arnold et al.*, 2015] and not being critical to aggregation in other RCE studies [*Muller and Held*, 2012].

Another approach to understanding the processes controlling column moisture and column moisture variance, whereby WTG balance is used to diagnose vertical motion from apparent heating [*Sobel et al.*, 2001; *Raymond*, 2001], has been implemented in recent analyses of the MJO [*Chikira*, 2014; *Janiga and Zhang*, 2016; *Wolding and Maloney*, 2015a]. This approach is consistent with the column MSE budget approach, and has the added benefit of allowing the vertical advection term of the column MSE budget to be quantitatively partitioned into contributions from various processes including radiative heating, microphysical processes, and subgrid scale (SGS) eddy transports. This approach is described briefly here, and in more detail in subsequent sections. The tropics are characterized by weak horizontal gradients of pressure and temperature, a consequence of effective gravity wave adjustment that occurs due to the relatively weak influence of planetary rotation near the equator. If variations in heating occur on spatial and temporal scales that allow effective gravity wave adjustment to occur, a first order balance between apparent heating and large-scale vertical advection of dry static energy (DSE) (i.e., adiabatic cooling) results. This balance is referred to as the WTG balance, and it proves useful in that it allows the large-scale vertical velocity to be diagnosed if both the apparent heating and static stability are known. Given the vertical moisture gradient, this vertical velocity can then be used to calculate the large-scale vertical moisture advection associated with an

apparent heating. Moreover, by considering the individual contributions of various apparent heating processes (i.e., microphysical processes, radiative heating, and SGS eddy transports) to the total apparent heating, the individual contributions of these processes to the total vertical moisture advection can be diagnosed. As highlighted by *Chikira* [2014], this approach has several advantages when compared to column integrated MSE budget analysis, including the ability to vertically resolve and more accurately assess the effect of various apparent heating processes on moisture. While vertically resolved WTG balance analyses have come to similar conclusions as column MSE analyses regarding the importance of longwave radiative feedbacks, they also highlight important information lost in column integrated analysis. For example, shortwave radiative heating anomalies associated with the MJO have a vertical dipole structure that, when vertically integrated, have a negligible impact on the column MSE budget. However, given the high moisture sensitivity of the lower troposphere to apparent heating [e.g., *Chikira*, 2014], shortwave radiative heating anomalies in the lower troposphere are associated with sizable moisture tendencies relevant to the moisture budget of the MJO [*Ma and Kuang*, 2011; *Wolding and Maloney*, 2015a; *Janiga and Zhang*, 2016]. The importance of such vertical structure to simulated convective aggregation is strongly supported by the results of *Muller and Bony* [2015], who showed that even when the column integrated radiative heating remained constant, aggregation was highly sensitive to the vertical profile of heating.

Here we present a vertically resolved WTG balance analysis of the MJO in the Superparameterized [*Grabowski*, 2001; *Randall et al.*, 2003] Community Earth System Model [*Hurrell et al.*, 2013] (SP-CESM), where temperature and moisture tendencies resulting from SGS eddy transports, microphysical processes, and radiative heating are addressed separately from large-scale advective transports. While the MJO is the focus of this paper, we would like to emphasize the applicability of such analysis techniques to more idealized studies of convective aggregation. In this study, we first aim to identify how various apparent heating processes contribute to the destabilization of the MJO. We then assess how the strength of various feedbacks differs between periods of low, moderate, and high MJO amplitude. Finally, a diagnostic approach to scale analysis is used to investigate the cause-effect relationship between apparent heating and large-scale motions at the heart of the WTG balance framework used throughout this study.

The paper is organized as follows. A description of the model and analysis techniques used in this study are provided in section 2. In section 3, composite moisture and moisture variance budgets are used to identify processes affecting large-scale moisture during established MJO events, and WTG balance analysis is used to explore the relationship between various apparent heating processes and large-scale vertical moisture advection. Periods of low, moderate, and high MJO amplitude are compared and contrasted in section 4, and the broader applicability of the WTG balance framework implemented in this study is explored in section 5. A comparison with previous studies is provided in section 6, and additional discussion and our conclusions are presented in section 7.

2. Model Description and Experimental Design

Superparameterization [*Grabowski*, 2001; *Randall et al.*, 2003] refers to the use of cloud system-resolving models (CSRMs), embedded within each column of a general circulation model (GCM), to compute tendencies of moisture and temperature resulting from processes occurring on the SGS of the GCM. When compared to conventional parameterizations, the explicit simulation of deep convection, fractional cloudiness, and cloud overlap that occurs in superparameterization allows for more realistic interactions between radiation, clouds, and the large-scale environment to occur. This may be one reason why models implementing super-parameterization have proved exceptionally adept at producing MJO-like variability [*Grabowski*, 2004; *Benedict and Randall*, 2009; *Stan et al.*, 2010; *Andersen and Kuang*, 2012; *Arnold et al.*, 2015; *Arnold and Randall*, 2015] when compared to conventionally parameterized GCMs [*Lin et al.*, 2006].

Superparameterization couples large-scale dynamics, SGS advective transports (i.e., cloud dynamics and turbulence), microphysics, and radiative transfer in such a way that their individual contributions to large-scale tendencies of moisture and temperature are cleanly separable, providing a unique framework that is ideal for this investigation. In this study, the atmospheric component of the Community Earth System Model (CESM) [*Hurrell et al.*, 2013] version 1.0.2 is the NCAR Community Atmosphere Model (CAM) run at $1.9° \times 2.5°$ horizontal resolution, with 30 vertical levels, CAM4 physics, and a 15 min time step. A two-dimensional CSRM, the System for Atmospheric Modeling (SAM) version 6 [*Khairoutdinov and Randall*, 2003], with a single moment bulk

microphysics scheme, 32 columns of 4 km width, and 28 vertical levels, is embedded within each CAM column and run with a 20 second time step. At each model level, a large-scale advective forcing that is calculated at each GCM timestep is applied evenly (both horizontally and temporally) to the CSRM domain as it subcycles through a sequence of shorter timesteps spanning the longer GCM timestep. At the end of the CSRM subcycling (i.e., the next CAM timestep), domain averaged changes in moisture and temperature resulting from microphysical processes and CSRM scale advection are applied in the host CAM, effectively acting as a parameterization of sub CAM grid scale processes. As SAM implements period boundary conditions, only vertical advective transports can contribute to changes in domain averaged moisture and temperature at each level. Radiative transfer occurs in each CSRM grid column at each CSRM timestep, although radiative transfer calculations are only done on GCM timesteps using time-averaged SAM fields. The atmospheric components of the SP-CESM are coupled to dynamic ocean (POP2) and sea ice (CICE) models with $1.125° \times 0.63°$ resolution.

We have chosen to analyze the 10 year preindustrial CO_2 (280 ppm) simulation of *Arnold et al*. [2015], as this simulation produced a realistic MJO whose basic features are well documented by *Arnold et al*. [2015], allowing more focus to be placed on the WTG balance analysis in this manuscript. Additionally, this simulation will allow a direct comparison of the vertically resolved WTG balance analysis and the column integrated MSE analysis, which was implemented by *Arnold et al*. [2015]. As sometimes occurs in models that produce vigorous intraseasonal variability [*Kim et al*., 2011], several mean state biases are present in this simulation. Worth highlighting is that model SST exhibits an approximate 1 K cold bias across the Indian Ocean and west Pacific relative to observations, has mean easterly low level winds across the Indian Ocean and Maritime Continent during boreal winter, and has a boreal winter precipitation maximum shifted too far west in the Indian Ocean. Further details and discussion of the simulation, including mean state biases and the structure of intraseasonal variation produced by this simulation, are provided in *Arnold et al*. [2015].

The moisture budget analyses of a composite "snapshot" of the MJO are produced from 19 wintertime (October to April) MJO events, selected using an index of $20-100$ day bandpass filtered OLR (not limited to eastward propagating wavenumbers), averaged over the area of $10°N-10°S$, $110°E-130°E$. Events were defined as index minima separated by at least 20 days, where anomalously low OLR (i.e., enhanced convection) caused the index to exceed a 1.5 standard deviation threshold. Results of composite "snapshots" will then be generalized using a moisture variance budget.

ERAi reanalysis [*Dee et al*., 2011], provided by the European Center for Medium-Range Weather Forecasts (ECMWF), will supplement the results of the SP-CESM analysis throughout this manuscript. These data were obtained at 6 h $1.5° \times 1.5°$ resolution for the years 1979–2012. ERAi moisture budget terms were calculated from the 6 hourly data, vertically integrated from the surface to 100 hPa, and then averaged to daily, unless otherwise indicated. The Filtered MJO OLR (FMO) index [*Kiladis et al*., 2014] is also used in the analysis of ERAi data. The FMO index and the EOFs used in its calculation can be obtained from http://www.esrl.noaa.gov/psd/mjo/mjoindex/.

An all season OLR based EOF index of the MJO is used in the moisture variance analysis of SP-CESM data. The leading EOFs of latitudinally averaged (15°N-15°S) 20-100 day bandpass filtered OLR were computed following the methodology that *Kiladis et al*. [2014] used to produce the FMO index. The first two EOFs explain 16.7% and 12.4% percent of the total variance respectively, and are well separated based on the criteria of *North et al*. [1982]. The structure of these EOFs, shown in Figure 1, is consistent with the structures of the OLR components of the multivariate EOF derived by *Wheeler and Hendon* [2004, Figure 1].
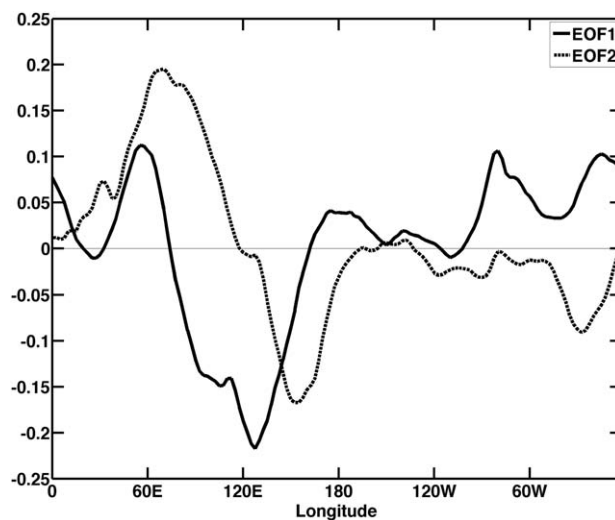

Figure 1. The two leading EOF structures of latitudinally averaged (15°N-15°S) 20-100 day bandpass filtered OLR for SP-CESM. The first two EOFs explain 16.7% and 12.4% percent of the total variance respectively.

In section 5, wavenumber-frequency filtering is used in the estimation of the characteristic magnitude of various terms. To compute spectra, data were divided into 49 overlapping subsets, each with a length of 144 days. The mean and linear trend were removed from each subset, and a Hann window was then applied. Each subset was converted in wavenumber-frequency space, limited to a single wavenumber-frequency combination, and then transformed back into longitude-time space. The characteristic magnitude of a given variable χ that has been filtered to a specific wavenumber-frequency combination (ω, λ) is estimated by its root mean squared modulus

$$[\chi^2]^{\frac{1}{2}}(\omega, \lambda) = \left(\frac{1}{L_x L_y T} \int_0^T \int_0^{L_y} \int_0^{L_x} \chi^2(x, y, t, \omega, \lambda); dx\, dy\, dt \right)^{\frac{1}{2}} \tag{1}$$

Each term was squared, and then the average taken over all longitudes, time and all subsets before taking the square root to arrive at a characteristic magnitude of the term for a given wavenumber-frequency combination. This was done for each individual latitude, and results were then averaged over latitudes spanning $3°N-3°S$, where WTG dynamics should be most apparent due to the smallness of the Coriolis force. This process was repeated for each wavenumber-frequency combination. This was done using data at the 525 hPa level, which is taken to be representative of the free troposphere and is near the level of maximum heating anomalies.

3. WTG Balance Analysis of Established MJO Events

The aims of this section are to:

1. motivate the need for understanding intraseasonal variations in large-scale vertical motion
2. outline a simplified framework for understanding intraseasonal variations in large-scale vertical motion
3. identify the processes acting to stabilize and destabilize the MJO when it is established

As general characteristics of the mean state and intraseasonal variability of this SP-CESM simulation are well documented in *Arnold et al.* [2015], a similar analysis will not be repeated here. The reader is encouraged to review section 3 and Figures 1 through 5 of *Arnold et al.* [2015] in order to familiarize themselves with these characteristics. Figure 2, which shows total and MJO filtered (following *Wheeler and Kiladis* [1999]) precipitation variance, is provided here to facilitate referencing regions used in the moisture and moisture variance budgets.

3.1. Motivation From a Traditional Moisture Budget
We begin by considering the moisture budget in the form

$$\frac{\partial \bar{q}}{\partial t} = -\bar{V}_h \cdot \nabla \bar{q} - \bar{\omega} \frac{\partial \bar{q}}{\partial p} + \bar{M} - \frac{\partial \overline{\omega' q'}}{\partial p} \tag{2}$$

where the overbar and prime indicate the large-scale horizontal area average of a quantity and deviations from the area average respectively, V_h and ω are the horizontal and vertical winds respectively, q is specific
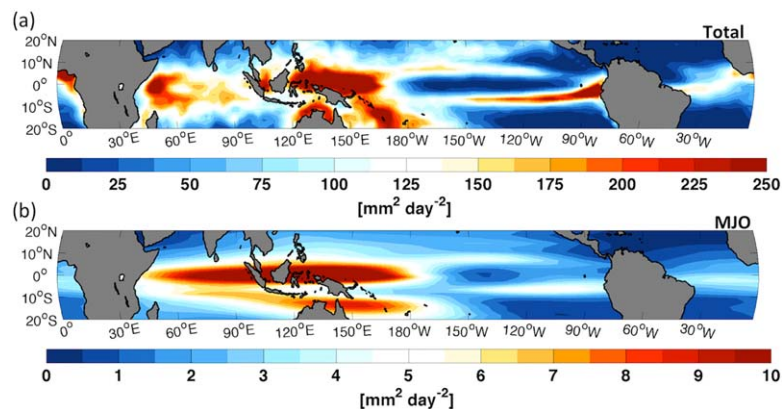

Figure 2. Variance of (a) unfiltered precipitation and (b) precipitation filtered to eastward wavenumbers 0 to 5 and frequencies corresponding to 20-100 days in SP-CESM.

humidity, M is the moisture tendency due to microphysical processes, and the term $-\nabla \cdot \overline{q'\boldsymbol{V}_h'}$ has been neglected. Note that the moisture tendency was calculated using a centered differences approach. Here "large-scale" refers to the approximately 200 km horizontal resolution of the CAM grid, which is large enough to contain an ensemble of clouds, but small enough to compromise only a small fraction of the MJO. Vertical eddy fluxes of moisture ($-\frac{\partial \overline{\omega'q'}}{\partial p}$) primarily represent the vertical redistribution of moisture by SGS cumulus convection [*Yanai and Johnson*, 1993], and reduce to surface fluxes of moisture when vertically integrated from the surface to tropopause if eddy fluxes of moisture through the tropopause are negligible. Note that the net effect of the last two terms in equation (2), which is calculated at the CRM scale and then applied to the GCM scale, is explicitly output by SP-CESM in this study. We will first present composite "snapshots" of each term in equation (2), taken when enhanced convection is centered near 120°E. Please note that the role some terms play (e.g., horizontal advection) is sensitive to the location at which the composites are based. To address this sensitivity, a moisture variance budget will subsequently be used to generalize many of the results obtained from these "snapshot" composites.

Figure 3 shows a composite moisture budget of 19 wintertime (October 1 to April 30) MJO events, where each term in equation (2) has been bandpass filtered to 20−100 days (denoted by the subscript $_{MJO}$ in this and subsequent figures) and averaged from 5°N−5°S. Specific humidity anomalies, given by the contours in each plot, indicate that the entire depth of the free troposphere is anomalously moist from ∼110°E−150°E, coincident with enhanced convection and reduced OLR (not shown). A shallow tongue of enhanced moisture extends eastward across the dateline, above which the troposphere remains anomalously dry. The moisture tendency (Figure 3a) indicates further moistening along the low level moisture tongue near and east of the dateline, while moisture anomalies between ∼120°E−170°E appear to be extending upward while simultaneously being eroded from below. Substantial drying throughout the depth of the troposphere is apparent over the Indian Ocean. Horizontal advective drying (Figure 3b) is enhanced across the entire eastern hemisphere, with the strongest drying centered around 700 hPa. Worth noting is that the largest specific humidity anomalies, occurring near 650 hPa, are coincident with a near zero moisture tendency despite enhanced horizontal advective drying. This indicates that some other process or set of processes must be acting as an anomalous moisture source in this region. Large-scale vertical moisture advection and the net effect of microphysical processes and SGS eddy moisture fluxes (Figures 3c and 3d respectively, please note color scale) are large and opposing processes that are strongest in the region of enhanced convection. While these processes result in a large degree of cancellation, anomalous moistening by large-scale vertical moisture advection slightly exceeds the anomalous drying effect of the latter processes (Figure 3e) in many regions. The incomplete cancellation of these processes, which is the focus of the subsequent section and was referred to as the column process in *Chikira* [2014], results in a net moistening that begins along the shallow tongue of enhanced moisture and then tilts westward with height, and opposes the enhanced advective drying occurring where moisture anomalies are largest. The budget residual (Figure 3f), calculated as the difference between the left and right hand side of equation (2), is small relative to the individual budget terms, providing confidence in the assessment provided here.

In summary, it appears that during the enhanced phase, large-scale vertical moisture advection provides more moisture than is removed by process occurring on the SGS (i.e., microphysics and SGS eddy fluxes), resulting in a net moistening which is opposed by horizontal advective drying. But why should it be that large-scale vertical moisture advection exceeds the moisture removed by processes acting on the SGS? A simplified framework for understanding vertical motion in the tropics will be used to address this question.

3.2. Vertically Resolved WTG Balance Framework and Analysis
Just as the quasi-geostrophic omega equation provides a useful simplified framework for understanding vertical motion in midlatitudes, WTG balance may, when applicable, provide a useful simplified framework for understanding vertical motion in the tropics [*Sherwood*, 1999; *Sobel et al.*, 2001; *Grabowski and Moncrieff*, 2004; *Chikira*, 2014; *Wolding and Maloney*, 2015a; *Janiga and Zhang*, 2016]. As WTG balance will play a fundamental role in the remainder of this paper, a primary goal of this paper is to be as transparent as possible regarding the physical interpretation of WTG balance in the context of the MJO. This section aims to show the utility of using WTG balance for understanding the MJO. A more detailed discussion of the applicability of WTG balance, and its physical interpretation in the context of the MJO, is provided in section 5.

Neglecting $-\nabla \cdot \overline{s'\boldsymbol{V}_h'}$, the DSE budget is given by
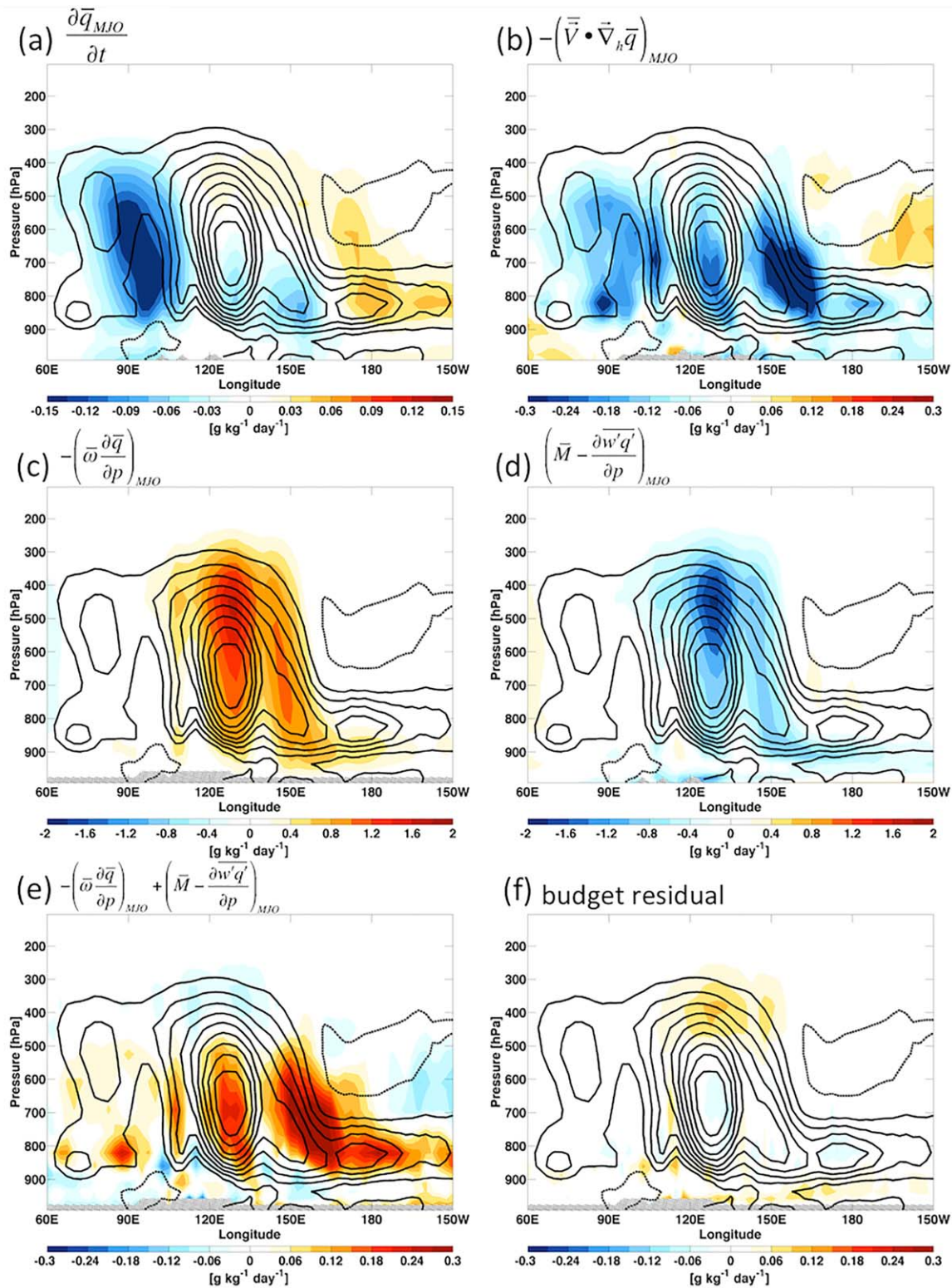
Figure 3. Longitude-height sections of latitudinally averaged (5°N-5°S) composite intraseasonal moisture budget terms (shading). These terms are the (a) Eulerian moisture tendency, (b) horizontal moisture advection, (c) vertical moisture advection, (d) the net effect of the microphysical moisture tendency and subgrid scale vertical eddy moisture flux convergence, (e) the column process (i.e., the sum of Figures 3c and 3d), and (f) the moisture budget residual. Solid and dashed contours indicate positive and negative specific humidity anomalies respectively, with contour intervals of 0.1 gkg^{-1}. Composites are produced from 19 independent wintertime (October 1 to April 30) events. Grey hatching indicates regions where data have been lost as a result of proximity to the surface. The subscript MJO indicates application of 20–100 day bandpass filtering. Please note the color scale differs between plots.
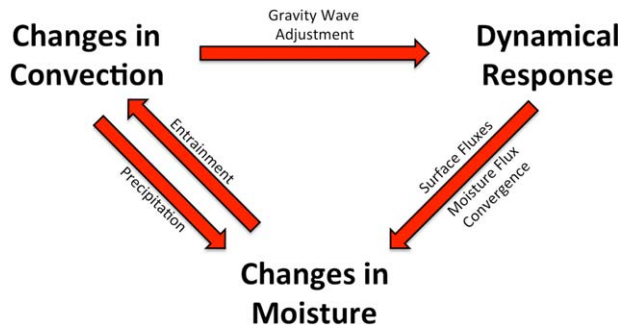
Under Weak Temperature Gradient Balance

Figure 4. A simplified schematic illustrating the relationship between various processes as viewed from the idealized weak temperature gradient balance framework adopted in this study.

$$\frac{\partial \bar{s}}{\partial t} + \bar{V}_h \cdot \nabla \bar{s} + \bar{\omega} \frac{\partial \bar{s}}{\partial p} = Q_1 \tag{3}$$

where the apparent heat source (Q_1) [*Yanai et al.*, 1973] is

$$Q_1 = \bar{Q}_M + \bar{Q}_R - \frac{\partial \overline{\omega' s'}}{\partial p} \tag{4}$$

and Q_M and Q_R are the DSE tendency due to microphysics and radiation respectively. WTG balance refers to a first order balance between large-scale vertical DSE advection and apparent heating, where the DSE tendency and horizontal DSE advection are lower order terms [*Sobel et al.*, 2001]. This balance is given by

$$\bar{\omega} \frac{\partial \bar{s}}{\partial p} = Q_1 \tag{5}$$

which can be rearranged to give

$$\bar{\omega} = \frac{Q_1}{\frac{\partial \bar{s}}{\partial p}} \tag{6}$$

In the context of the MJO, this paper takes the perspective that intraseasonal variations in large-scale vertical motion are a direct dynamical response to variations in apparent heating. This balance results because effective gravity wave adjustment occurs on temporal scales much shorter than, and spatial scales much larger than, intraseasonal variations in apparent heating. The utility of equation (6) is that it can be used to relate large-scale vertical moisture advection to apparent heating, such that

$$-\bar{\omega} \frac{\partial \bar{q}}{\partial p} = \frac{1}{L_v} \left(\bar{\alpha} Q_1 \right) \tag{7}$$

where

$$\bar{\alpha} = -L_v \left(\frac{\frac{\partial \bar{q}}{\partial p}}{\frac{\partial \bar{s}}{\partial p}} \right) \tag{8}$$

Note that $\bar{\alpha}$, originally introduced by *Chikira* [2014], can be thought of as the sensitivity of large-scale vertical moisture advection to apparent heating, where the static stability determines the vertical motion resulting from some apparent heating, and the vertical moisture gradient determines the amount of moistening or drying that results from that vertical motion. This paper takes the perspective that moisture, through convective scale processes such as entrainment, acts as the intermediary through which the dynamical response to apparent heating can, in turn, influence subsequent apparent heating, thereby allowing for potential positive feedbacks to occur. This perspective is summarized in Figure 4, and essentially considers the MJO to be a slowly moving Matsuno-Gill pattern maintained by positive feedbacks between moisture, apparent heating, and large-scale dynamics. Note that, from this perspective, processes fundamental to the MJO span from the scale of turbulence (e.g., entrainment) to the planetary scale dynamical response, highlighting the challenges in simulating and understanding the MJO.

Figures 5a and 5b show SP-CESM $\bar{\alpha}$ lowpass filtered (denoted by the subscript $_{LP}$ in this and subsequent figures) to 20 days, and bandpass filtered to $20-100$, respectively. Moisture sensitivity to apparent heating is largest in the lower troposphere and decreases monotonically with height, largely a result of the sharp decrease in the vertical moisture gradient with height. Intraseasonal moisture variations result in a reduction of $\bar{\alpha}$ at low levels and an increase in $\bar{\alpha}$ at upper levels during the enhanced phase, which will be shown to be important in subsequent sections.
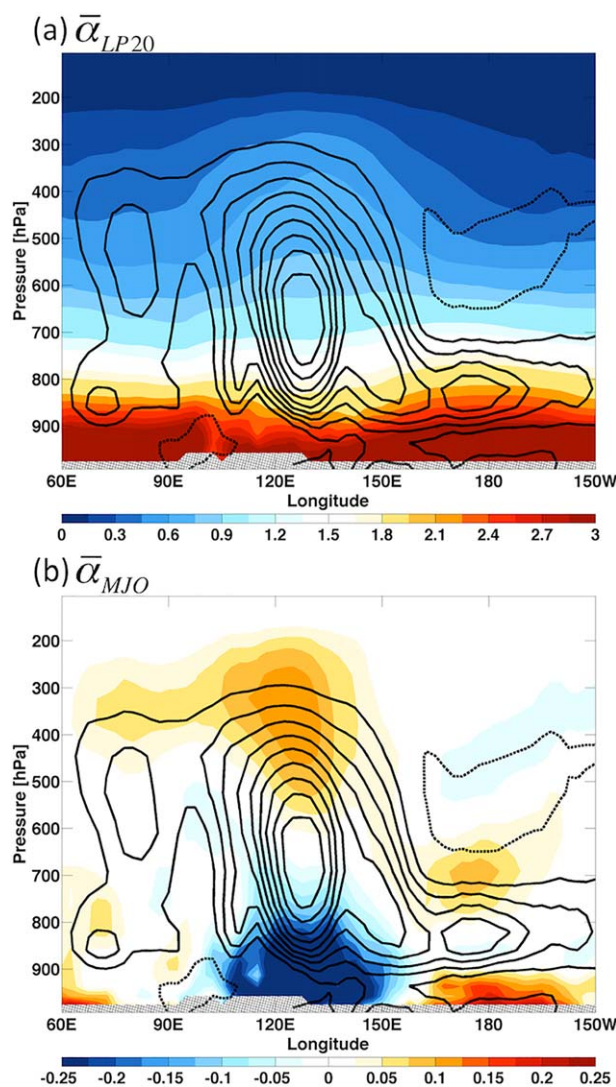
Figure 5. As in Figure 3, except the color shading indicates alpha, where alpha has been (a) lowpass filtered to 20 days and (b) bandpass filtered to 20–100 days. The subscripts LP20 and MJO indicate application of 20 day lowpass and 20–100 day bandpass filtering respectively. Please note the color scale differs between plots.

A reasonable "first check" on the WTG balance assumption is to assess the degree to which intraseasonal variations in large-scale vertical motion can actually be diagnosed from apparent heating. Figure 6 shows the actual large-scale vertical velocity and vertical moisture advection (Figures 6a and 6b), that diagnosed using WTG balance (Figures 6c and d), and the difference between the two (Figures 6e and 6f). Figure 6g is the same as Figure 6f, except a different color scale is used to better highlight the structure of errors in the WTG balance diagnosis. Note that, to incorporate the effects of higher frequency variability (i.e., variability occurring on timescales less than 20 days), a 3 day lowpass filter has been used in the WTG diagnosis (Figures 6e and 6f). This contrasts the 20 day lowpass filter used in the WTG diagnosis of *Wolding and Maloney* [2015a, Figure 6], and results in an improvement of the WTG estimates of large-scale vertical velocity and vertical moisture advection. The WTG diagnosis of vertical motion and vertical moisture advection is exceptionally accurate throughout the free troposphere. As may be expected, the WTG balance diagnosis does not work as well below 900 hPa. Given this, a conservative limit of 850 hPa is applied to subsequent analyses dependent upon the WTG balance framework, and grey hatching will be applied below 850 hPa in plots which rely on the WTG balance framework. Now that a simplified framework for understanding intraseasonal variations in vertical motion is in place, the contributions that various apparent heating processes make to vertical moisture advection can be assessed.

Figure 7a shows the "direct" effect of SGS processes (i.e., microphysics and SGS eddy fluxes) on large-scale moisture content. This is the same as Figure 3d, where only the color scale has been changed to highlight weaker moisture tendencies. The strong drying effect of increased precipitation processes during the enhanced phase is evident. Figure 7b shows the large-scale heating that results from these same SGS processes. Please note that this heating does not include the effects of radiation. The similar structures of drying and heating in Figures 7a and 7b respectively highlight the dominant role that microphysical processes play in each, though more subtle differences are evident, owing in part to differences in SGS eddy transports of moisture and DSE [*Yanai et al.*, 1973]. The heating in Figure 7b, through large-scale adjustment, contributes to large-scale vertical moisture advection, shown in Figure 7c. This can be thought of as the "indirect" effect (i.e., WTG balance effect) of SGS processes on large-scale moisture content. The structure of moistening in Figure 7c is much more bottom heavy than the structure of heating in Figure 7b, reflecting the higher moisture sensitivity of the lower troposphere to apparent heating. When the direct and indirect effects of SGS processes on large-scale moisture content are considered together, shown in Figure 7d, their incomplete cancellation results in substantial moistening at low levels to the east of enhanced convection that helps drive the eastward propagation of moisture anomalies in this region. Note that Figure 7d is the
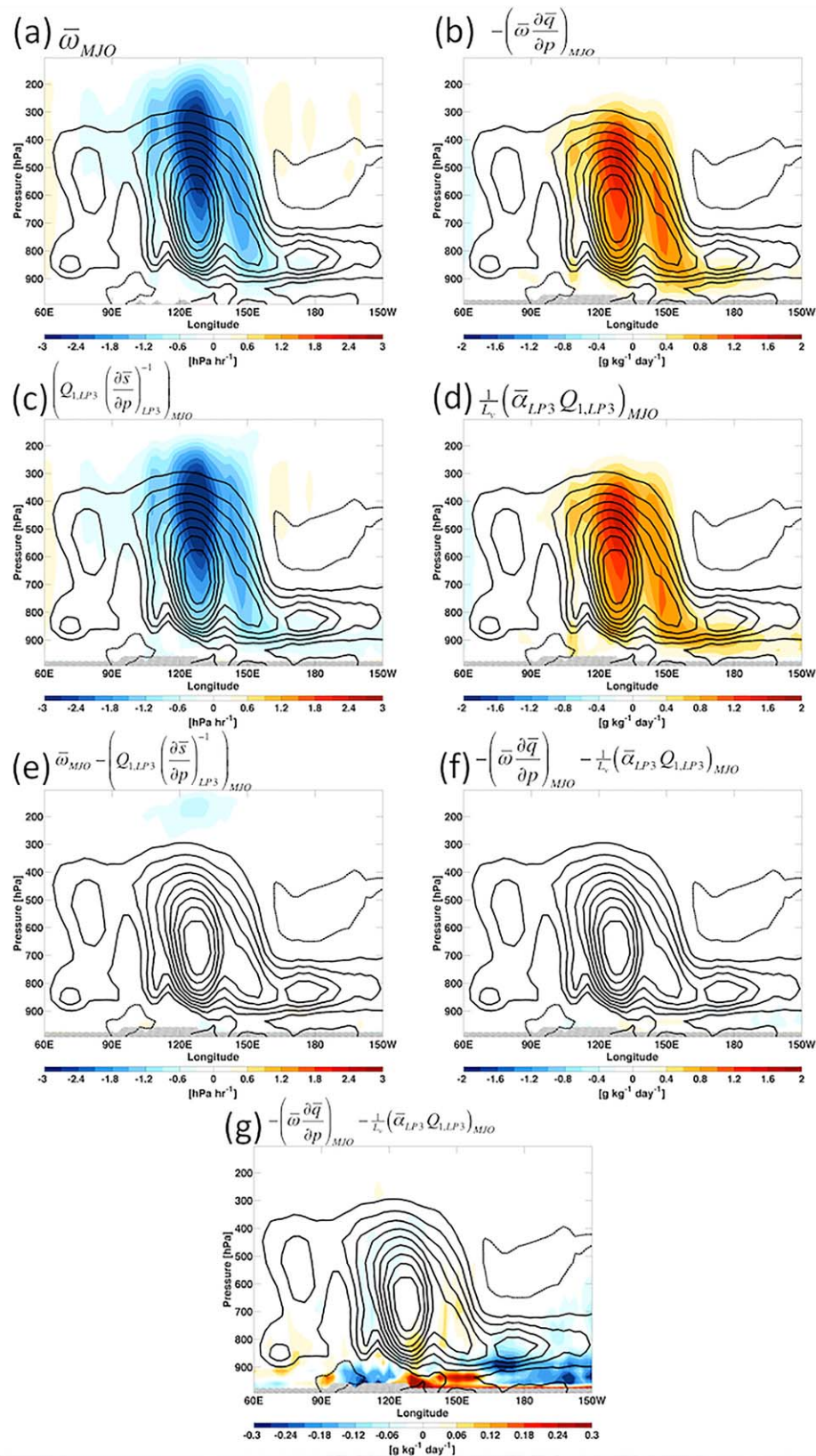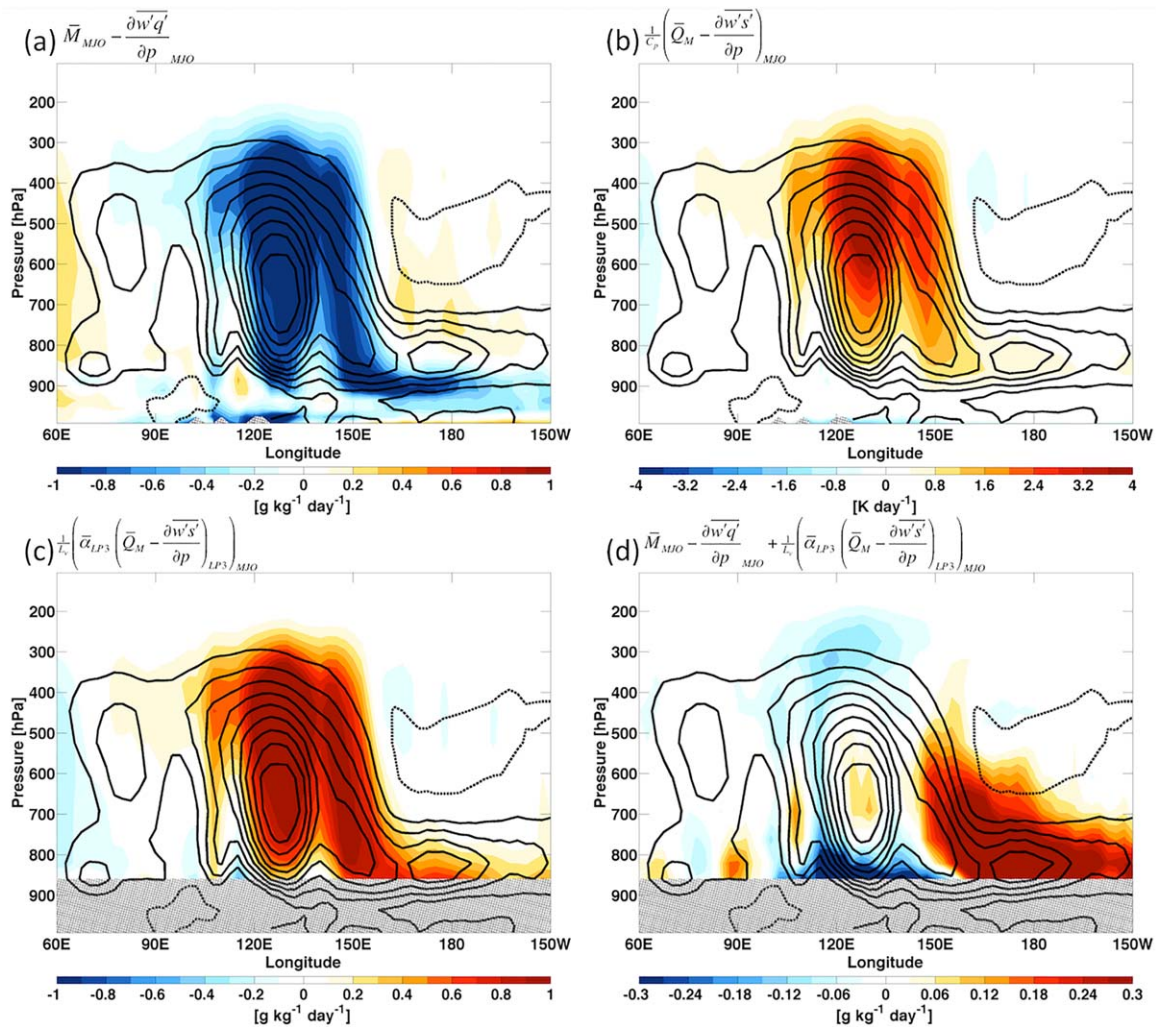
Figure 6.

Figure 7. As in Figure 3, except the color shading indicates (a) the net effect of the microphysical moisture tendency and subgrid scale (SGS) vertical eddy moisture flux convergence, (b) the net effect of microphysical heating and SGS vertical eddy heat flux convergence, (c) the large-scale vertical moisture advection associated with the aforementioned heating (i.e., Figure 7b) under weak temperature gradient balance, and (d) the sum of the direct and weak temperature gradient balance moisture tendencies associated with microphysical processes and SGS vertical eddy flux convergence (i.e., the sum of Figures 7a and 7c respectively). Grey hatching has been applied below 850 hPa in Figures 7c and 7d, as weak temperature gradient balance in not applicable in the boundary layer. The subscripts LP3 and MJO indicate application of 3 day lowpass and 20–100 day bandpass filtering respectively. Please note the color scale differs between plots.

same as the column process (Figure 3f) without the "indirect" effects of radiative heating on large-scale moisture. Interestingly, while drying is evident at lower and upper levels in the region of enhanced convection, the incomplete cancellation of the direct and indirect effects of these processes results in a net moistening at mid levels in the region of enhanced convection, where the largest moisture anomalies are observed. Note that the effects of surface flux variations are included in Figure 7. The vertical integral of these processes will be considered in the subsequent section, thereby allowing the effects of convection to be separated from the influence of surface latent heat flux (SLHF) feedbacks.

Figure 8 shows total, longwave, and shortwave radiative heating anomalies (Figures 8a, 8c, and 8e respectively), and the large-scale vertical moisture advection (Figures 8b, 8d, and 8f respectively) they drive under WTG balance. Intraseasonal variations in total radiative heating appear to be sufficient to compensate for

Figure 6. As in Figure 3, except the color shading indicates the anomalous (a) large-scale vertical velocity and (b) vertical moisture advection in SP-CESM, the anomalous (c) large-scale vertical velocity and (d) vertical moisture advection diagnosed using weak temperature gradient balance assumptions, and the difference between the actual and diagnosed (e) large-scale vertical velocity and (f, g) vertical moisture advection. The subscripts LP3 and MJO indicate application of 3 day lowpass and 20-100 day bandpass filtering respectively. Please note the color scale of Figure 6g differs from that of Figures 6b, 6d, and 6f.
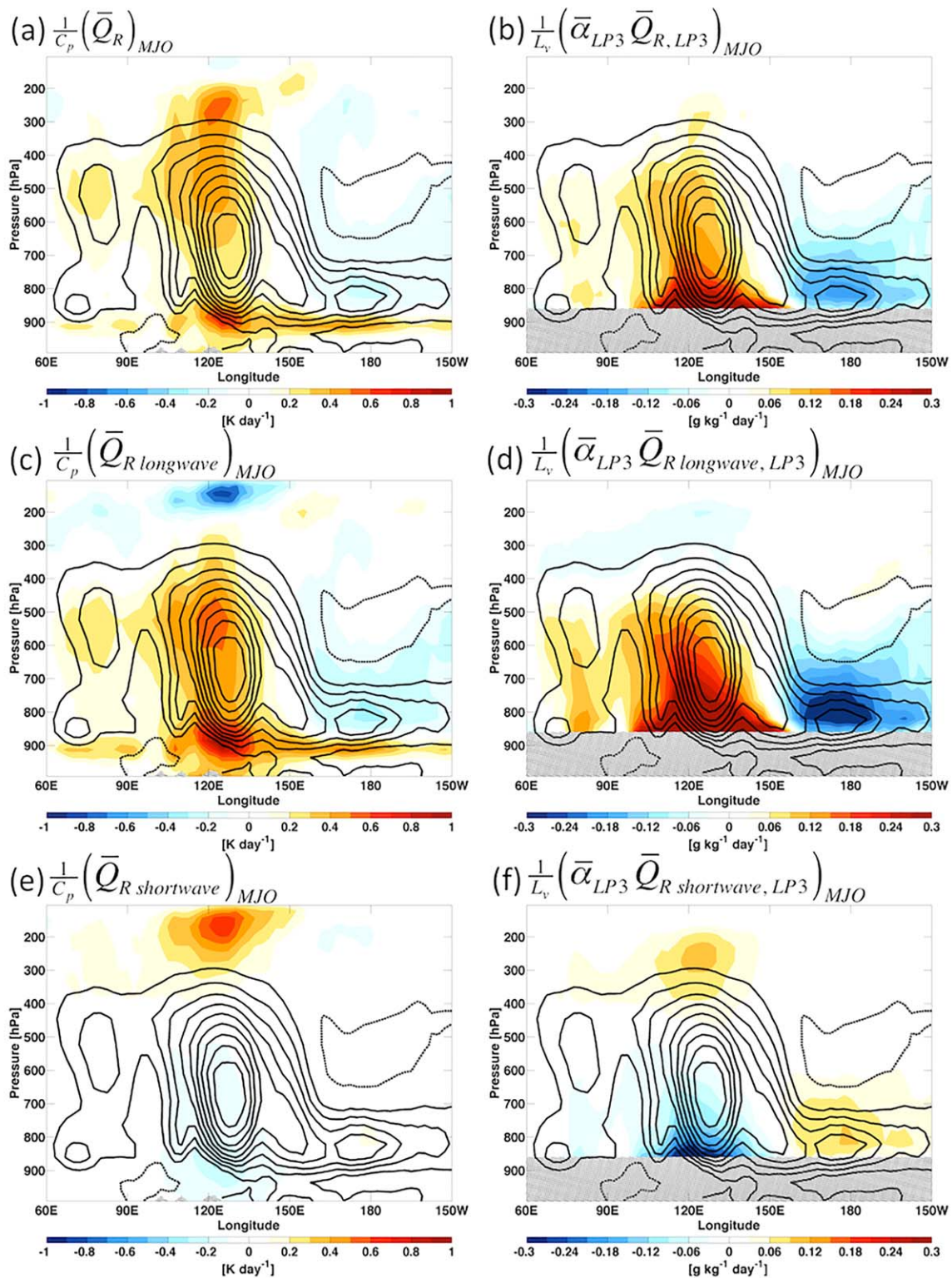
Figure 8. As in Figure 3, except the color shading indicates anomalous (a) total, (c) longwave, and (e) shortwave radiative heating, and the corresponding (b, d, f) large-scale vertical moisture advection diagnosed using weak temperature gradient balance. Grey hatching has been applied below 850 hPa in Figures 8b, 8d, 8f, as weak temperature gradient balance in not applicable in the boundary layer. The subscripts LP3 and MJO indicate application of 3 day lowpass and 20–100 day bandpass filtering respectively.

the low level drying seen in Figure 7d, and contribute to the mid level moistening seen in Figure 3e. Total radiative heating anomalies result from opposing changes in longwave and shortwave terms, the latter of which has a distinct vertical dipole structure. In the middle and lower troposphere, the reduction of long-wave cooling during the enhanced phase is substantially stronger than the reduction of shortwave heating. Yet it is worth highlighting that the low level moisture tendency associated with variations in shortwave heating is not negligible when compared with other moisture budget terms such as horizontal advection.

In this section, a simplified framework for understanding intraseasonal variations in large-scale vertical motion has been used to highlight the role various apparent heating processes play in driving large-scale vertical moisture advection. It is worth highlighting that composites used in this and previous sections (e.g., Figure 3) only provide information about a single phase of the MJO lifecycle at a given geographical location. The next section will employ an approach that considers the entire lifecycle of the MJO over a broad geographic region.

3.3. Moisture Variance Budget of the MJO

In the previous section, intraseasonal variation in large-scale vertical moisture advection in the tropics were shown to be closely related to convective activity under WTG balance. Given this close relationship, subsequent discussion will often focus on the net effect of large-scale vertical moisture advection, microphysical processes, and SGS eddy fluxes. In order to aide discussion of these processes, their net effect will hereafter be referred to as the column process [*Chikira*, 2014]. In this section, an intraseasonal moisture variance budget will be used to more objectively assess the role that various moisture budget terms play in the destabilization and propagation of the MJO.

The fractional growth rate of intraseasonal column moisture variance contributed by moisture budget term P is given by

$$G_P(p,t) = \frac{\int\int P(p)\langle q\rangle dx\,dy}{\int\int \langle q\rangle^2 dx\,dy} \tag{9}$$

where specific humidity has been bandpass filtered to $20-100$ days, and the angled brackets represent vertical integrals from the surface to 100 hPa. Similarly, the fractional contribution of a moisture budget term P to the column moisture tendency is given by

$$T_P(p,t) = \frac{\int\int P(p)\langle\frac{\partial q}{\partial t}\rangle dx\,dy}{\int\int \langle\frac{\partial q}{\partial t}\rangle^2 dx\,dy} \tag{10}$$

Here the domain considered is $10°N-14.5°S, 60°E-180°E$, and subsequent figures are averaged over the 30 days preceding and following each of the 19 winter events composited in Figure 3, for a total of 1159 days. The moisture variance tendency was computed by projecting the moisture tendency, calculated using a centered differences approach, onto the column moisture anomalies, as in equation (9). Equations (9) and (10) warrant further discussion. In these equations, the choice was made to project moisture budget term P (p) onto the column integrated terms $\langle q\rangle$ and $\langle\frac{\partial q}{\partial t}\rangle$. An alternative approach could be to project moisture budget term $P(p)$ onto the anomalous moisture and moisture tendency at each level, $q(p)$ and $\frac{\partial q(p)}{\partial t}$ respectively, and to subsequently consider the vertical integral of the product of those terms. While both methods were investigated in this study, the former was chosen on the basis that the SGS effects of convection can vertically redistribute moisture provided by other processes (e.g., radiative heating), such that their influence is distributed throughout the column.

Figure 9a shows vertical profiles of how various moisture budget terms contribute to the growth or reduction of intraseasonal column moisture variance over the entire MJO lifecycle. This can be interpreted as follows. If a term has a positive growth rate at a given level, this indicates that term is moistening that level when the column is anomalously moist, and drying that level when the column is anomalously dry. Each term has been scaled by the mass equivalent of 900 hPa, the depth over which the column moisture anomalies are calculated. This is done in order to obtain a growth rate per unit time (per day), and can be interpreted as the column moisture variance growth rate (i.e., increase or decrease in aggregation) that would result from the moisture budget term at that level acting over the depth of the troposphere. Very little growth exists in domain averaged moisture variance over the period considered here (black solid line), which is the result of an
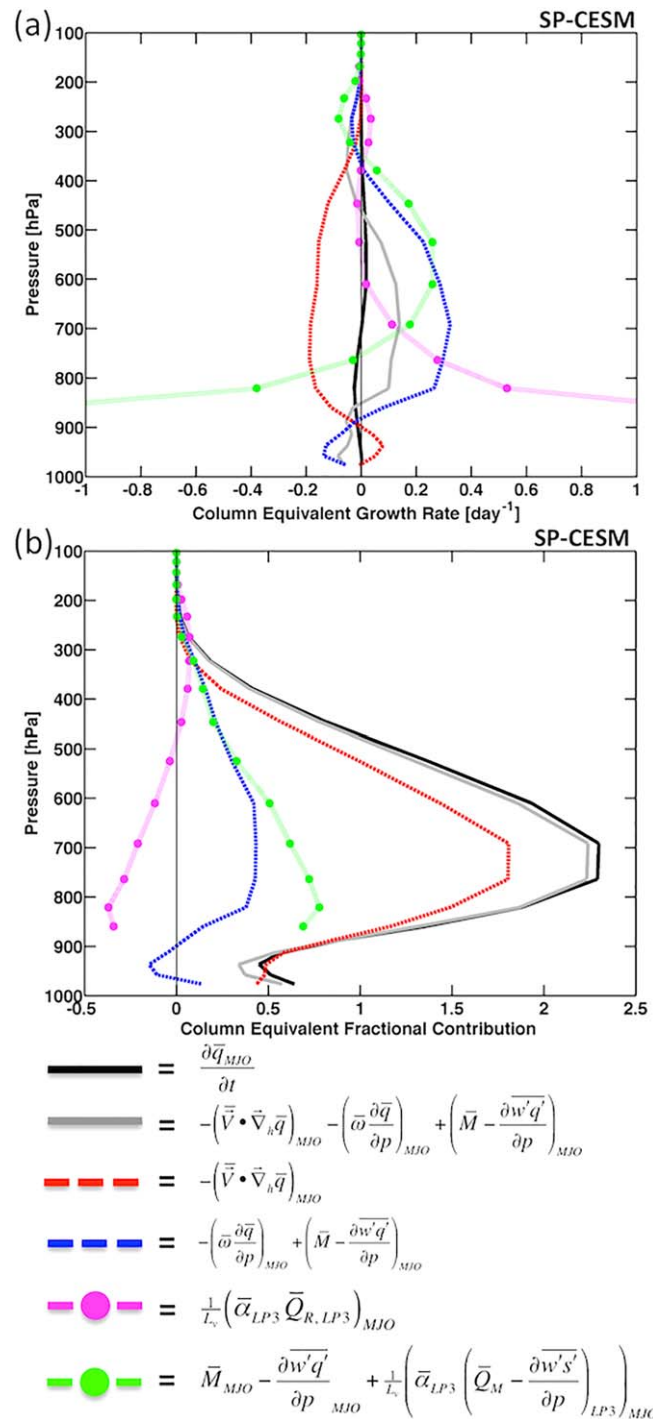
Figure 9. Vertical profiles of contributions various budget terms make to the (a) column moisture variance growth rate and (b) column moisture tendency in SP-CESM, corresponding to equations (9) and (10) respectively. Column moisture was calculated by vertically integrating from the surface to 100 hPa. The area weighted integral has been taken from 10.5°N-14.5°S, 60°E-180°E, and averaged from day −30 to day +30 for each of the 19 independent winter events composited. In order to ease interpretation, each term has been scaled by the mass equivalent of 900 hPa at each level. The subscripts LP3 and MJO indicate application of 3 day lowpass and 20-100 day bandpass filtering respectively.

approximate balance between moisture variance growth (i.e., destabilization) by the column process (blue dashed line) and the reduction of moisture variance (i.e., damping) by horizontal advection (red dashed line). Both of these terms act fairly uniformly between 850 and 500 hPa. Using the WTG balance framework, the column process can be decomposed into contributions from total radiative heating (magenta dot-dashed line) as well as the net effect of microphysical processes and SGS eddy fluxes (green dot-dashed line). Total radiative heating makes large contributions to column moisture variance, acting almost exclusively below 600 hPa. Interpretation of the net effect of microphysical processes and SGS eddy fluxes is more difficult, as SGS eddy fluxes have the ability to redistribute moisture vertically. It is therefore not possible to identify specific levels where column moisture variance is actually being reduced. It seems likely that much of the negative growth rate occurring at low levels in this term represents SGS eddy fluxes vertically redistributing the moisture anomalies provided by radiative heating variations (green dot-dashed line) at low levels to mid and upper levels. Consideration of the mass weighted vertical integral of this term, which will be done shortly, provides much more insight.

Figure 9b shows vertical profiles of how various moisture budget terms contribute to the intraseasonal column moisture tendency (i.e., propagation of the MJO) over the entire MJO lifecycle. Again, each term has been scaled by the mass equivalent of 900 hPa, and can be interpreted as the fractional contribution to the column moisture tendency that would result from the moisture budget term at that level acting over the depth of the troposphere. As may be expected, propagation of column moisture anomalies results primarily from processes occurring at low to mid levels, where moisture anomalies are largest (Figure 3). While this results primarily from horizontal advection (red dashed line), the column
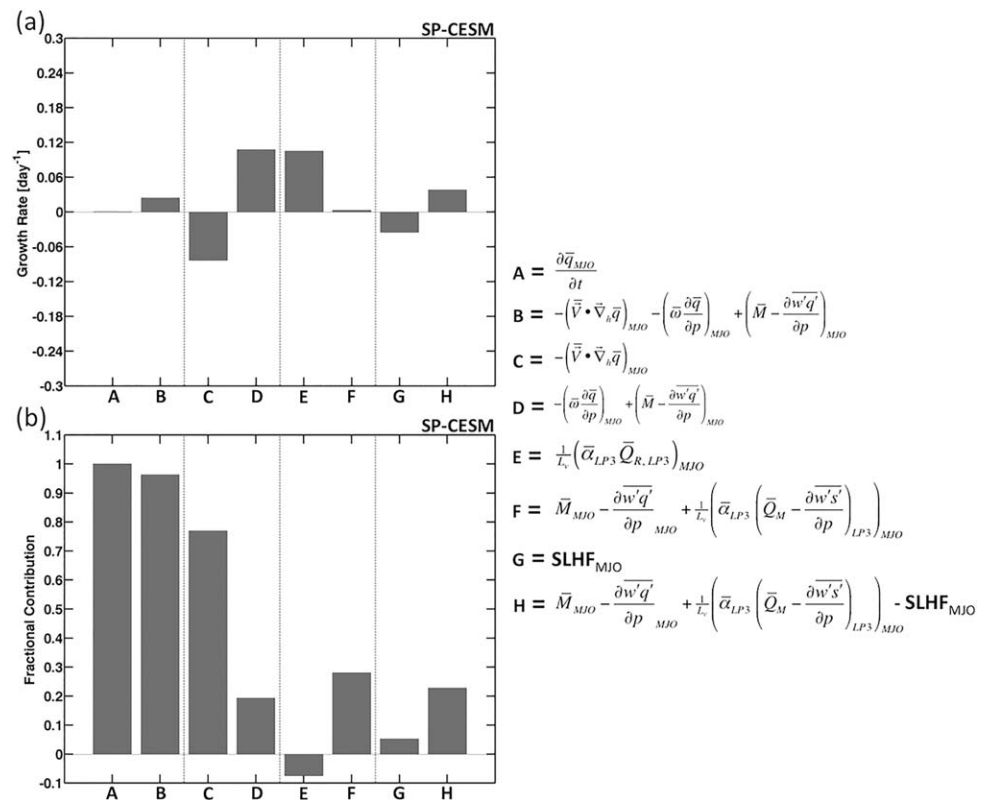
Figure 10. Vertically integrated contributions various budget terms make to the (a) column moisture variance growth rate and (b) column moisture tendency in SP-CESM, corresponding to the vertical integral of equations (9) and (10), respectively. Column moisture was calculated by vertically integrating from the surface to 100 hPa, as were terms A through D. Terms E, F, and H were vertically integrated from 850 to 100 hPa, as they depend on the weak temperature gradient approximation. The area weighted integral has been taken from 10.5°N-14.5°S, 60°E-180°E, and averaged from day −30 to day +30 for each of the 19 independent winter events composited. The subscripts LP3 and MJO indicate application of 3 day lowpass and 20–100 day bandpass filtering respectively.

process (blue dashed line) also plays a significant role. Contributions from the column process are almost exclusively the result of the net effect of microphysical processes and SGS eddy fluxes (green dot-dashed line), and are weakly opposed by total radiative heating variations (magenta dot-dashed line).

Figures 10a and 10b show the results of taking the mass weighted vertical integral of equations (9) and (10), and are equivalent to taking the vertical average of each term in Figures 9a and 9b respectively. Given their dependence on WTG balance, terms E, F, and H have only been vertically integrated from 850 to 100 hPa. These levels of vertical integration will be applied to all terms that rely on WTG balance in subsequent figures. Please note that, while a conservative lower limit was applied here, WTG balance may prove to be applicable even lower. Figure 10a shows the total growth rate of intraseasonal column moisture variance that results from various moisture budget terms. Again, the column moisture variance growth rate (Term A) is small over the period considered here, a result of the large degree of cancellation between destabilization by the column process (term D) and damping by horizontal advection (Term C).

Terms E and F show the decomposition of the column process (Term D) into contributions from total radiative heating as well as the net effect of microphysical processes and SGS eddy fluxes respectively. It is worth highlighting that term F can be further decomposed into contributions from variations in surface fluxes of moisture (Term G) and SGS convective processes (Term H, i.e., convection in the absence of radiative and surface flux feedbacks). SGS convective processes (Term H) are destabilizing in SP-CESM, and this destabilization is strongly reenforced by variations in radiative heating (Term E). The results of *Arnold and Randall* [2015], who found that MJO-like variability persisted when cloud-radiative feedbacks were removed in their global aquaplanet simulation using SP-CESM, support the finding that SGS convective processes alone (i.e.,
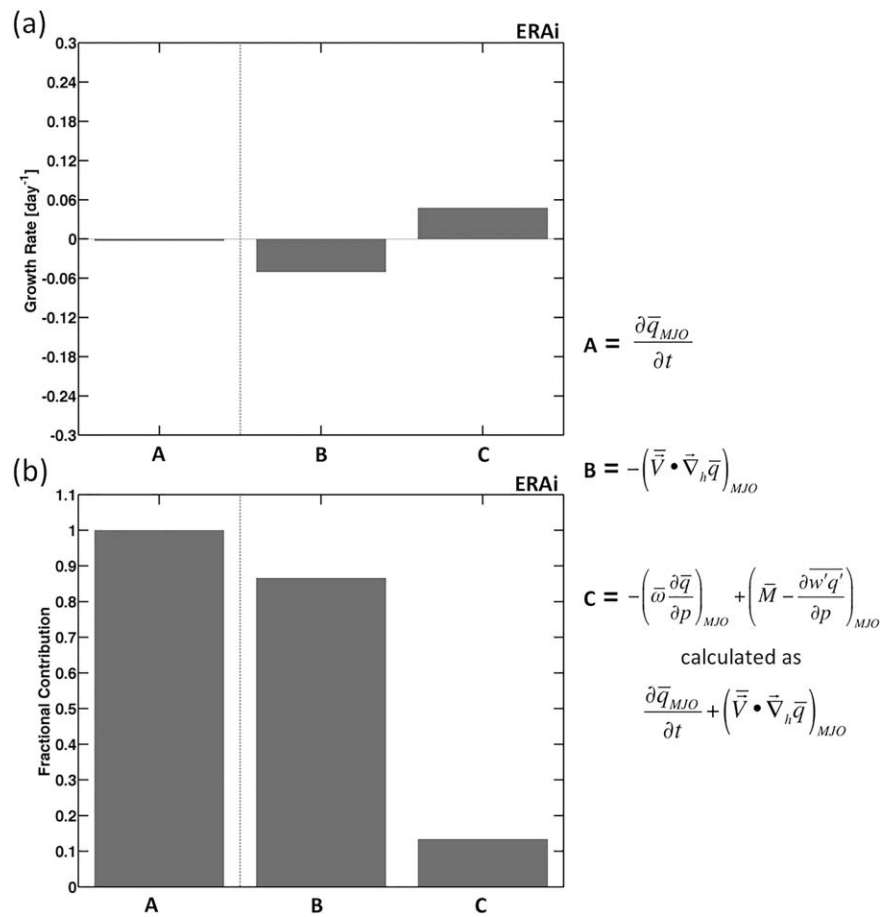
Figure 11. As in Figure 10, except for ERA-interim reanalysis data. The area weighted integral has been taken from 10.5°N-13.5°S, 60°E-180°E, and averaged over every winter (1 October to 30 April) day where the magnitude of the FMO index exceeded a value of 1. The subscript MJO indicates application of 20–100 day bandpass filtering.

in the absence of radiative and surface flux feedbacks) have a destabilizing effect in SP-CESM. SLHF feedbacks (Term G) are actually a stabilizing process in SP-CESM, owing to the mean state easterlies that prevail over the Indian Ocean and Maritime Continent. Figures 10b reiterates that the propagation of the MJO is primarily driven by horizontal advection, with the net effect of microphysical processes and SGS eddy fluxes playing a secondary, though still important, role.

In order to highlight similarities and differences between the MJO in SP-CESM and the MJO in the real world, a similar albeit more limited analysis has been produced using ERAi reanalysis data, as shown in Figure 11. These terms were calculated over the domain of $10.5°N-13.5°S, 60°E-180°E$, and averaged over every winter (1 October to 30 April) day where the magnitude of the FMO index exceeded a value of 1. Lack of closure of the ERAi moisture budget is thought to be the result of poor estimations of terms associated with the column process (e.g., precipitation, large-scale vertical moisture advection) [*Morita et al.*, 2006; *Benedict and Randall*, 2007; *Lau and Wu*, 2010; *Kiranmayi and Maloney*, 2011; *Sobel et al.*, 2014; *Kim et al.*, 2014b; *Wolding and Maloney*, 2015a]. This motivated calculating the ERAi column process as the residual of Eulerian moisture tendency and horizontal advection. As ERAi produces a fairly realistic representation of intraseasonal moisture variations [*Tian et al.*, 2010], this essentially amounts to an assumption that intraseasonal variation in horizontal moisture advection are well represented in ERAi. Comparing Figures 10 and 11 suggests that the same balance of processes occurs in SP-CESM as in the real world MJO, with the most notable difference being the dramatically higher growth rates occurring in SP-CESM. This suggests that the MJO may be more unstable in SP-CESM than in the real world, and is consistent with the findings of *Arnold et al.* [2015], who showed that intraseasonal OLR variance in SP-CESM is substantially larger than that in observations.
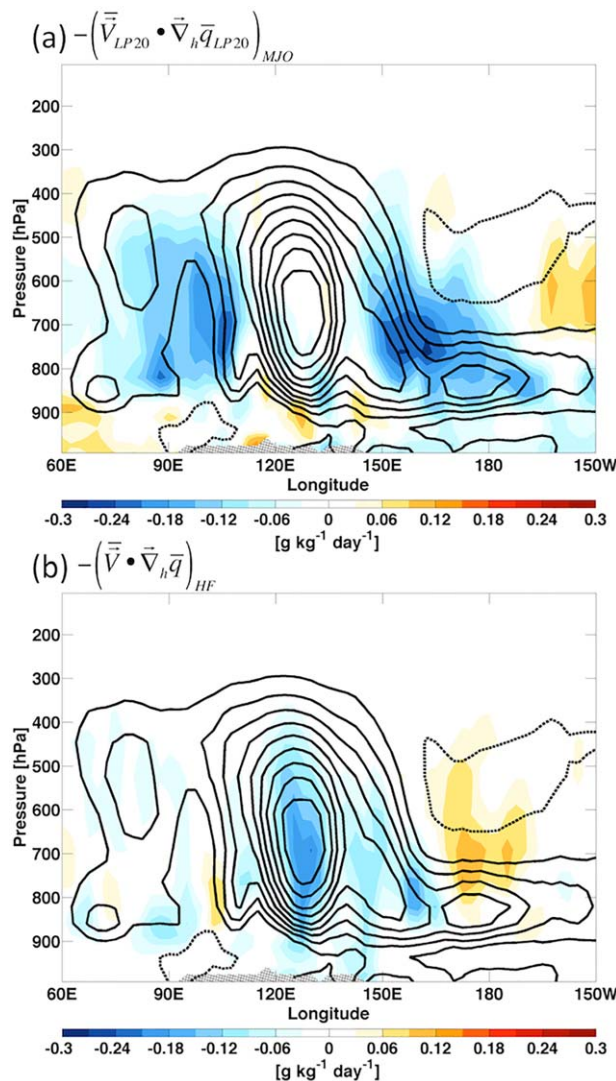
Figure 12. As in Figure 3, except the color shading indicates horizontal moisture advection due to (a) slow variations and (b) higher frequency variability (as indicated by the subscript HF) calculated following equation (12). The subscripts LP20 and MJO indicate application of 20 day lowpass and 20–100 day bandpass filtering respectively.

3.4. The Role of Higher Frequency Variability

Several observational and modeling studies have shown that the intraseasonal modulation of higher frequency convective variability (e.g., convectively coupled equatorial waves and TD-type disturbances) results in substantial horizontal advective diffusion or damping of moisture anomalies [*Maloney and Dickinson*, 2003; *Maloney*, 2009; *Maloney et al.*, 2010; *Kiranmayi and Maloney*, 2011; *Andersen and Kuang*, 2012; *Chikira*, 2014]. In this section, the role higher frequency convective variability plays in driving both horizontal advective damping and large-scale vertical moisture advection will be investigated.

As in *Chikira* [2014], horizontal advection can be decomposed as

$$-(\bar{\boldsymbol{V}}_{\boldsymbol{h}} \cdot \nabla \bar{q})_{\mathrm{MJO}} = -(\bar{\boldsymbol{V}}_{\boldsymbol{h},\mathrm{LP20}} \cdot \nabla \bar{q}_{\mathrm{LP20}})_{\mathrm{MJO}}$$
$$-(\bar{\boldsymbol{V}}_{\boldsymbol{h}} \cdot \nabla \bar{q})_{\mathrm{HF}} \qquad (11)$$

where

$$(\bar{\boldsymbol{V}}_{\boldsymbol{h}} \cdot \nabla \bar{q})_{\mathrm{HF}} = (\bar{\boldsymbol{V}}_{\boldsymbol{h},\mathrm{LP20}} \cdot \nabla \bar{q}_{\mathrm{HP20}})_{\mathrm{MJO}}$$
$$+ (\bar{\boldsymbol{V}}_{\boldsymbol{h},\mathrm{HP20}} \cdot \nabla \bar{q}_{\mathrm{LP20}})_{\mathrm{MJO}}$$
$$+ (\bar{\boldsymbol{V}}_{\boldsymbol{h},\mathrm{HP20}} \cdot \nabla \bar{q}_{\mathrm{HP20}})_{\mathrm{MJO}} \qquad (12)$$

and the subscript $_{\mathrm{HP20}}$ indicates the application of 20 day highpass filtering. The first term on the right hand side of equation (11) represents horizontal advection resulting from the slowly varying wind field acting on the slowly varying moisture field, while the second term on the right hand side results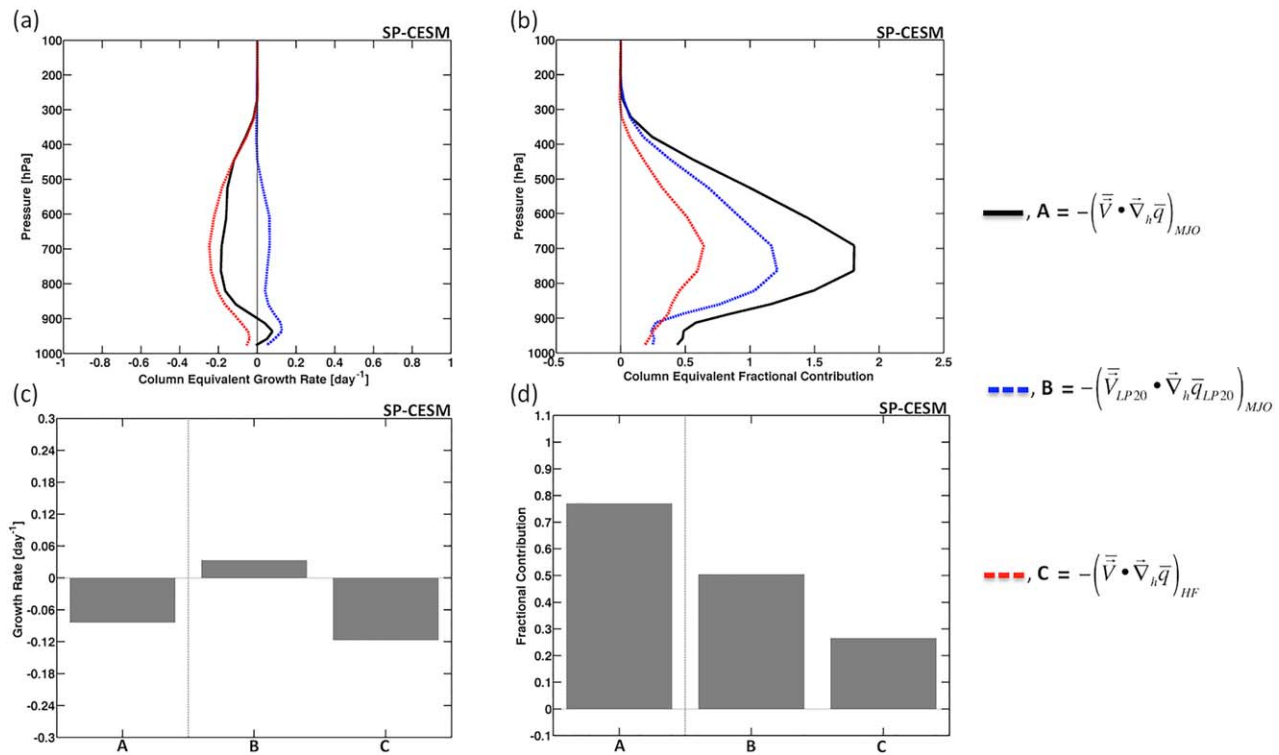 from the presence of higher frequency variability. These terms will be referred to as horizontal advection by slowly varying fields and higher frequency variability respectively.

Figures 12a and 12b show the decomposition of horizontal moisture advection (Figure 3b) into horizontal advection by slowly varying fields and higher frequency variability respectively. Horizontal advection by slowly varying fields results in drying at the eastern and western periphery of the moisture anomalies, while horizontal advection by higher frequency variability results in considerable drying where the moisture anomalies are largest. Figure 13 shows the moisture variance analysis of these terms, which considers their effect throughout the entire lifecycle of the MJO over a broad geographic region. Figures 13a and 13c indicate that horizontal advection damping results solely from presence of higher frequency variability (red dashed line, Term C), and that horizontal advection by slowly varying fields (blue dashed line, Term B) contributes weakly to moisture variance growth. Figures 13b and 13d suggest that horizontal advection by slowly varying fields (blue dashed line, Term B) plays a more dominant role in driving propagation of the MJO than horizontal advection by higher frequency variability (red dashed line, Term C).

Figure 13. (a, b) As in Figure 9a, and (c, d) as in Figure 10a, except for various horizontal advective terms. The subscripts LP20 and MJO indicate application of 20 day lowpass and 20-100 day bandpass filtering respectively. The subscript HF indicates terms related to higher frequency variability, calculated following equation (12).

Using WTG balance, large-scale vertical moisture advection can be decomposed as

$$-\left(\bar{\omega}\,\frac{\partial \bar{q}}{\partial p}\right)_{MJO} = \frac{1}{L_v}\left(\left(\bar{\alpha}_{LP20}\,Q_{1,LP20}\right)_{MJO} + \left(\bar{\alpha}\,Q_1\right)_{HF}\right) \tag{13}$$

where

$$\left(\bar{\alpha}\,Q_1\right)_{HF} = \left(\bar{\alpha}_{LP20}\,Q_{1,BP3-20}\right)_{MJO} + \left(\bar{\alpha}_{BP3-20}\,Q_{1,LP20}\right)_{MJO} + \left(\bar{\alpha}_{BP3-20}\,Q_{1,BP3-20}\right)_{MJO} \tag{14}$$

and the subscript $_{BP3-20}$ indicates the application of $3-20$ day bandpass filtering. The first term on the right hand side of equation (13) represents large-scale vertical moisture advection resulting from slowly varying heating acting in a moist thermodynamic environment with slowly varying $\bar{\alpha}$, while the second term on the right hand side results from the presence of higher frequency variability. These terms will be referred to as large-scale vertical moisture advection by slowly varying fields and higher frequency variability respectively.

Figures 14a and 14b show the decomposition of large-scale vertical moisture advection (Figure 3c) into contributions from slowly varying fields and higher frequency variability respectively. While slowly varying fields contribute the majority of the total large-scale vertical moisture advection, the contribution of higher frequency variability is still considerable, being similar in magnitude to horizontal advection and the column process (Figures 3b and 3e respectively). The last term on the right hand side of equation (14), $\left(\bar{\alpha}_{BP3-20}\,Q_{1,BP3-20}\right)_{MJO}$, is the dominant contributor to $\left(\bar{\alpha}\,Q_1\right)_{HF}$ (not shown). In order to determine how higher frequency variability contributes to large-scale vertical moisture advection, an index of $\left(\bar{\alpha}_{BP3-20}\,Q_{1,BP3-20}\right)_{MJO}$ integrated from 850 hPa to 100 hPa and averaged over the domain $10°N-10°S$, $70°E$ $-85°E$ was used to produce lag-day composites. A total of 81 winter time events, selected by choosing maxima separated by at least 5 days and exceeding 1.5 standard deviations from the time series of domain averaged $\left(\bar{\alpha}_{BP3-20}\,Q_{1,BP3-20}\right)_{MJO}$, were used to produce Figure 15. Figure 15a indicates that apparent heating by higher frequency convective variability peaks above the level of the largest moisture anomalies associated with the higher frequency variability. The moisture sensitivity to apparent heating (i.e., $\bar{\alpha}_{BP3-20}$, Figure 15b) has been increased at this level, a result of the higher frequency moisture anomalies. The
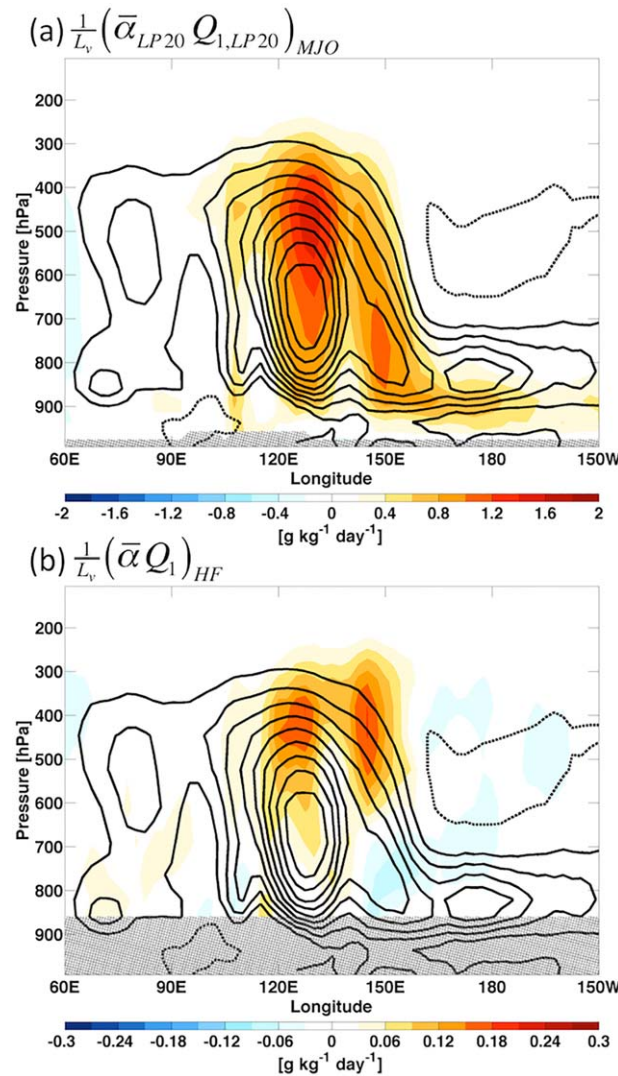
Figure 14. As in Figure 3, except the color shading indicates large-scale vertical moisture advection due to (a) slow variations and (b) higher frequency variability (as indicated by the subscript HF) calculated following equation (14). The subscripts LP20 and MJO indicate application of 20 day lowpass and 20–100 day bandpass filtering respectively.

covariance of higher frequency variations in apparent heating (Figure 15a) with higher frequency variations in $\bar{\alpha}$ (Figure 15b) result in considerable large-scale vertical advective moistening of the mid and upper troposphere (Figure 15c). Intraseasonal modulation of higher frequency convective activity, as documented by several previous studies [*Maloney and Dickinson*, 2003; *Maloney*, 2009; *Maloney et al.*, 2010; *Kiranmayi and Maloney*, 2011; *Andersen and Kuang*, 2012; *Chikira*, 2014], can therefore contribute to intraseasonal variations in large-scale vertical moisture advection.

Figure 16 shows a moisture variance analysis of the net effect of higher frequency convective variability (black line, Term A) decomposed into contributions from horizontal advection (blue dashed line, Term B) and large-scale vertical moisture advection (red dashed line, Term C). While large-scale vertical moisture advection driven by higher frequency convective variability offsets a considerable portion of the horizontal advective damping effect, the net effect of higher frequency convective variability is still to damp intraseasonal moisture variance.

3.5. Detailed Analysis of Large-Scale Vertical Moisture Advection by Slowly Varying Fields

Large-scale vertical moisture advection resulting from slowly varying fields can be decomposed into contributions resulting from intraseasonal variations in apparent heating acting on the background moist thermodynamic profile, background apparent heating rates acting on intraseasonal variations in the moist thermodynamic profile (Figure 5b), and intraseasonal variations in apparent heating acting on intraseasonal variations in the moist thermodynamic profile. This is decomposition is made as follows:

$$\frac{1}{L_v}\left((\bar{\alpha}_{LP20}\,Q_{1,LP20})_{MJO}\right) = \frac{1}{L_v}\left(\bar{\alpha}_{LP100}\,Q_{1,MJO} + \bar{\alpha}_{MJO}\,Q_{1,LP100} + \bar{\alpha}_{MJO}\,Q_{1,MJO}\right) \tag{15}$$

where the subscripts LP20, LP100, and MJO indicate application of 20 day lowpass, 100 day lowpass, and 20−100 day bandpass filtering respectively.

Figure 17 shows this decomposition applied to the longwave and shortwave radiative heating terms in the column moisture variance budget, where terms relating to intraseasonal variations in radiative heating acting on intraseasonal variations in the moist thermodynamic profile have been omitted because of their negligible contribution. First consider the column integrated effect of the various terms, as shown in Figure 17b. The total radiative heating term (term A) results almost entirely from the longwave radiative heating term (term B), and the shortwave radiative heating term (term C) results in only a small reduction of growth rate. To first order, the total radiative heating term (term A) can be described by the sum of intraseasonal
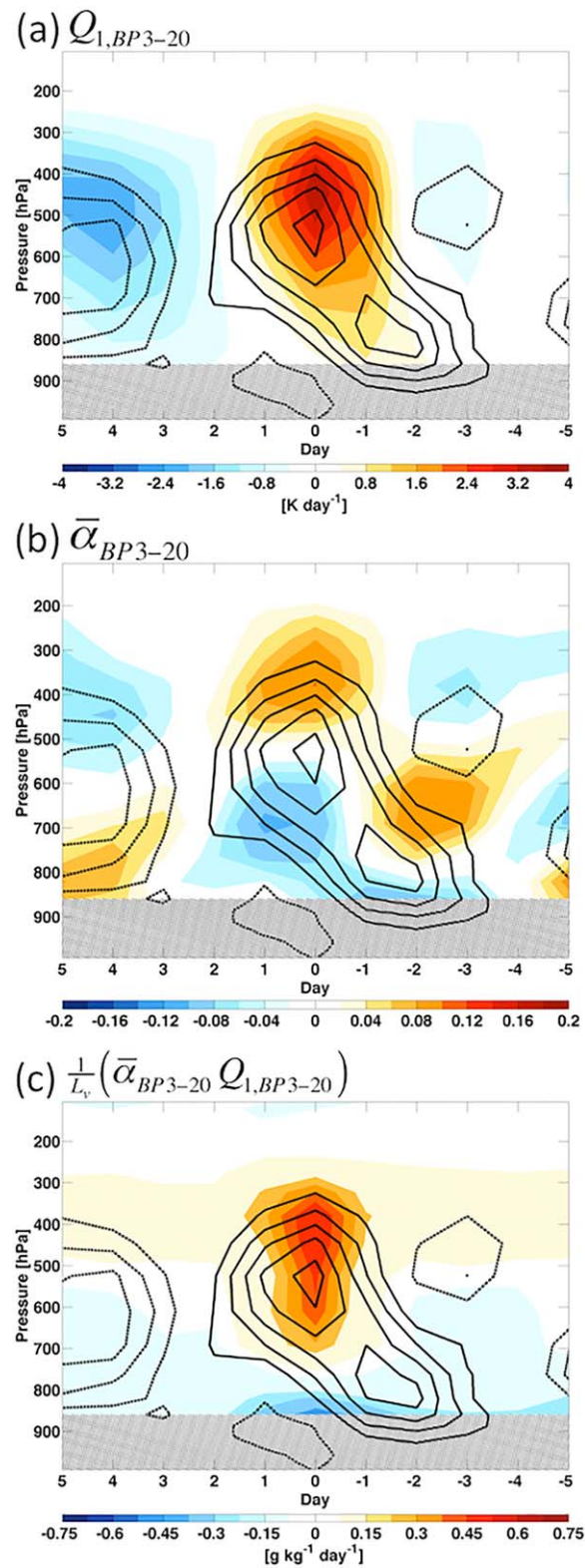
Figure 15. Vertical profiles of various terms relating to higher frequency convective activity (shading) as a function of lag-day. Solid and dashed contours indicate positive and negative specific humidity anomalies respectively, with contour intervals of 0.1 gkg^{-1}. Composites are produced from 81 independent wintertime (1 October to 30 April) events, and averaged over the domain 10°N-10°S, 75°E-85°E. See text for more details on the compositing method. Grey hatching has been applied below 850 hPa, as weak temperature gradient balance in not applicable in the boundary layer. The subscript BP3-20 indicates application of 3–20 bandpass filtering.
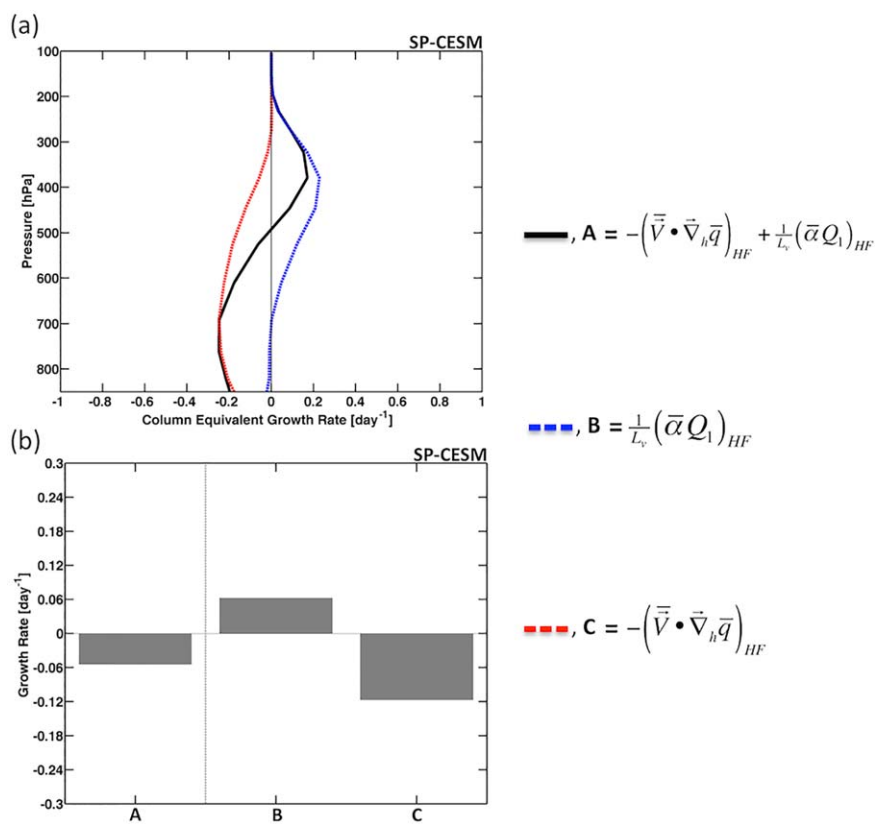
Figure 16. (a) As in Figure 9a, and (b) as in Figure 10a, except for terms related to higher frequency convective variability. The subscript HF indicates terms related to higher frequency variability, calculated following equations (12) and (14).

variations in longwave and shortwave heating acting on the background moist thermodynamic profile (terms D and F respectively). Background longwave and shortwave heating rates acting on intraseasonal variations in the moist thermodynamic profile (terms E and G) make relatively small contributions to the total radiative heating term (term A). Inspection of the vertical profiles of how each term contributes to column moisture variance (Figure 17a) provides a more nuanced perspective. Each of the longwave and shortwave terms make important contributions to the vertical structure of the moistening/drying that contributes to moisture variance growth. Throughout most of the column, intraseasonal variations in longwave heating acting on the background moist thermodynamic profile (blue dashed line) contribute to column moisture variance growth. While this profile is bottom heavy to begin with, background longwave heating acting on variations in the moist thermodynamic profile (green dot-dashed line) makes the total longwave heating term (black line) substantially more bottom heavy. Both of the shortwave heating terms (red dashed and magenta dot-dashed lines) act in such a way that their combined effect (grey line) is to make total radiative heating term (magenta dot-dashed line Figure 10a) substantially more top heavy than would result from the longwave heating term alone (black line).

Do changes in these vertical profiles matter if the column integral stays the same? In other words, does it matter where moistening or drying of the column occurs? As tropical convection is particularly sensitive to dry air entrainment below the freezing level [*Lucas et al.*, 1994; *Zipser*, 2003; *Sahany et al.*, 2012], it would seem that the addition or removal of moisture at low levels (i.e., more bottom heavy profiles) would have a larger influence on convection than that at upper levels (i.e., top heavy profiles). If this is true, longwave radiative feedbacks may be more destabilizing than their column integrated effect (i.e., Term B) would suggest. Similarly, shortwave radiative feedbacks may be more stabilizing than their column integrated effect (i.e., Term C) would suggest. Yet the extent to which SGS eddy fluxes quickly redistribute intraseasonal moisture anomalies in the vertical remains unclear, though it likely varies throughout the MJO lifecycle. This should be a topic of future research.
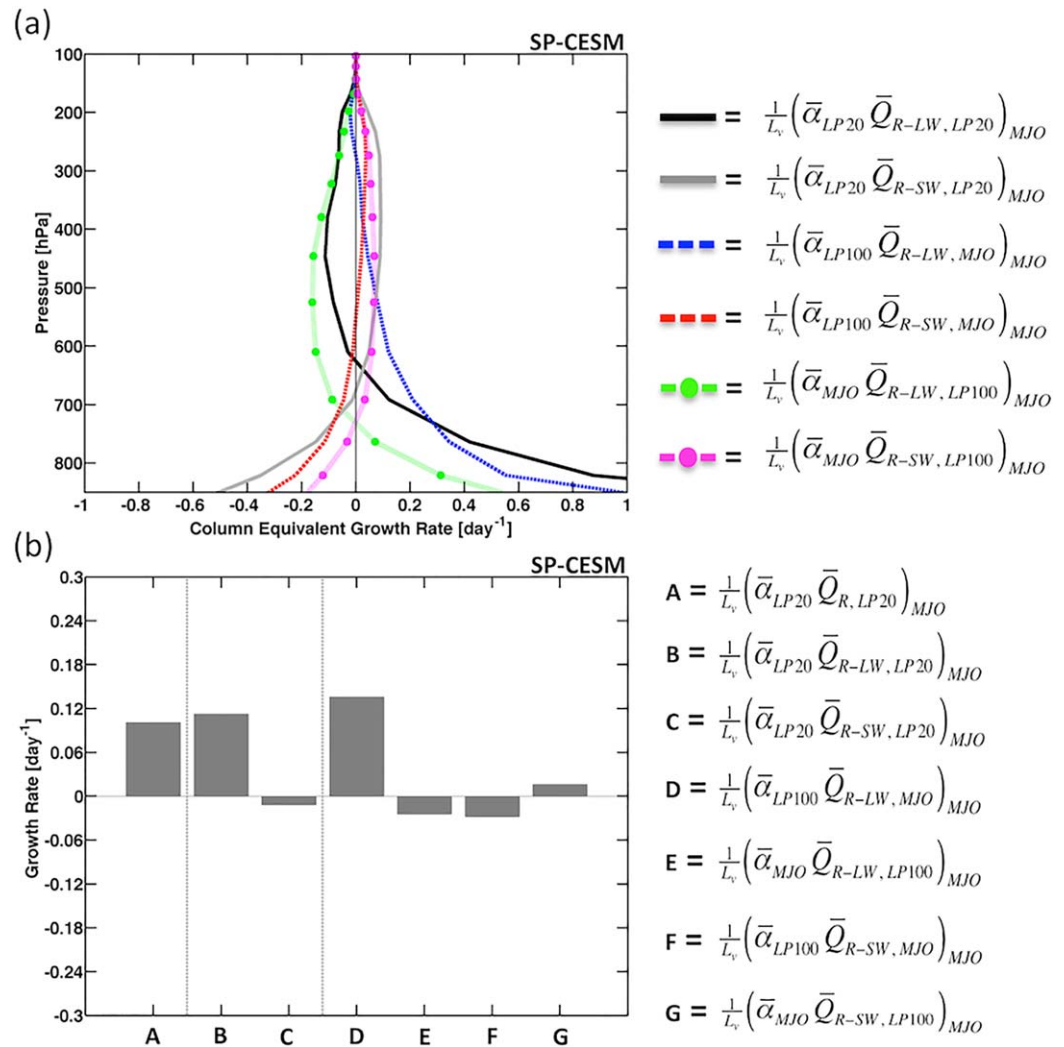
Figure 17. (a) As in Figure 9a, and (b) as in Figure 10a, except for various radiative heating terms. Each term in Figure 17b was vertically integrated from 850 to 100 hPa, as they depend on the weak temperature gradient approximation. The subscripts LP20, LP100, and MJO indicate application of 20 day lowpass, 100 day lowpass, and 20–100 day bandpass filtering respectively.

Figures 18a and 18b show various microphysical and SGS eddy flux terms of the column moisture variance budget, where the first three terms (black, blue, and red lines and terms A, B, and C) include the effects of both slowly varying fields and higher frequency activity, and the latter two terms (green and magenta lines and terms D and E) result only from slowly varying fields. All terms in 18b have been vertically integrated from 850 to 100 hPa. The total effect of microphysical processes and SGS eddy fluxes (black line) results from the sum of their direct effect on column moisture (blue dashed line) and their indirect effect (by producing large-scale vertical moisture advection) on column moisture (red dashed line, Term C). The direct effect of microphysical processes and SGS eddy flux includes the effect of SLHF variations, and therefore the black and blue dashed terms in Figure 18a include this SLHF effect. To address this, the effect of SLHF variations is subtracted from the vertical integral of these terms, as shown in Figure 18b. When the effects of SLHF variations are removed, the sum of the direct (Term B) and indirect (Term C) effects of microphysical processes and SGS eddy fluxes, which are large and opposing terms, results in modest growth of column moisture variance (Term A). Recall that this modest growth is strongly reenforced by the total radiative effect (Figure 17b, term A). As shown in the previous section, the indirect effect of microphysical processes and SGS eddy fluxes (Term C) is the result of slowly varying fields as well as higher frequency convective activity. The indirect effect of the slowly varying fields is primarily the result of intraseasonal variations in heating acting on the background moist thermodynamic profile (green dot-dashed line, term D), but
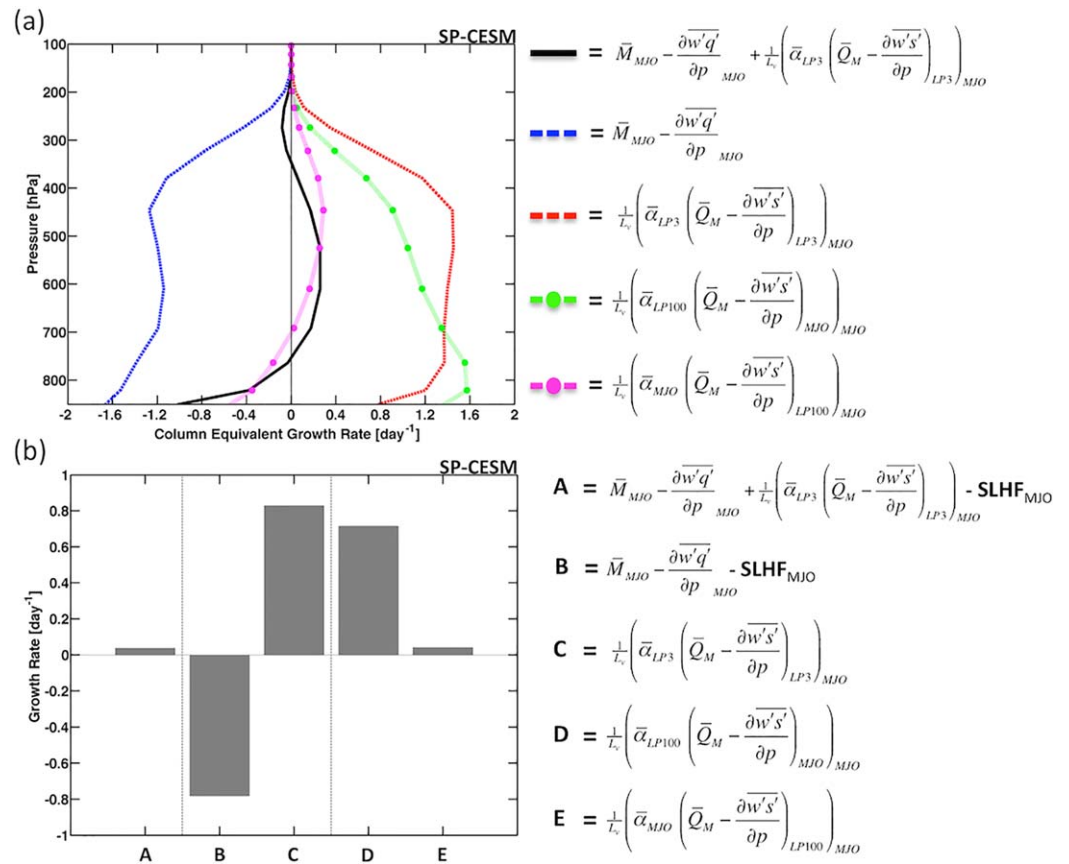
Figure 18. (a) As in Figure 9a, and (b) as in Figure 10a, except for various terms relating to microphysical processes and subgrid scale vertical eddy flux convergence. Each term in Figure 18b was vertically integrated from 850 to 100 hPa. The subscripts LP3, LP100, and MJO indicate application of 3 day lowpass, 100 day lowpass, and 20–100 day bandpass filtering respectively.

background heating acting on variations in the moist thermodynamic profile (magenta dot-dashed line, term E) results in a substantially more top-heavy profile. Intraseasonal variations in heating acting on intraseasonal variations in the moist thermodynamic profile (not shown) make a negligible contribution.

4. Limits to Growth of the MJO

The previous sections indicate that the MJO is destabilized by both SGS convective processes and radiative feedbacks, and that this destabilization is opposed by horizontal advective damping when the MJO is well established. How representative is this characterization of the MJO? Does destabilization by SGS convective processes and radiative feedbacks begin to saturate (i.e., become weaker) as the amplitude of the MJO increases? This section aims to answer these questions by assessing the strength of various feedbacks during periods of low, moderate, and high MJO amplitude.

Figures 19a and 19b show the results of moisture variance budgets for SP-CESM and ERAi respectively, where budgets for both data sets have been calculated during periods where their MJO indices (FMO-like and FMO respectively, see section 2 for details) have a magnitude between 0.75 and 1 (dark blue bars), 1 and 1.5 (light blue bars), 1.5 and 2 (green bars), 2 and 2.5 (yellow bars), and greater than 2.5 (red bars). Lower to higher values of these OLR-based MJO indices correspond with periods of time where MJO convective anomalies are weak and geographically limited (dark blue bars) and strong and widespread (red bars) respectively [*Wolding and Maloney*, 2015b]. Sample sizes are provided in the figure caption. In both SP-CESM and ERAi, destabilization by the column process (Term D) is greater during periods of high MJO amplitude (red bars) than during periods of low MJO amplitude (blue bars), and this increased destabilization is approximately balanced by an increase in horizontal advective damping (Term C). Figure 20 indicates that
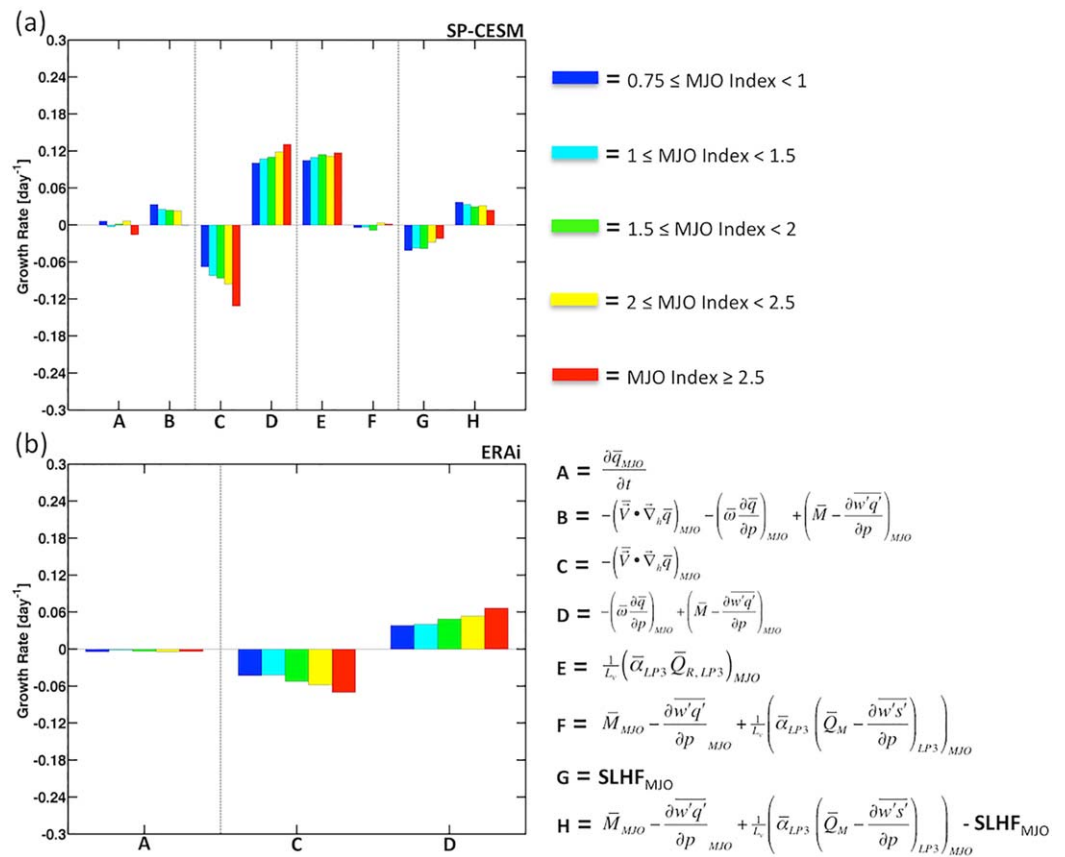
Figure 19. As in Figure 10a, except composited over wintertime periods when the magnitude of the MJO index was between 0.75 and 1 (dark blue bars), 1 and 1.5 (light blue bars), 1.5 and 2 (green bars), 2 and 2.5 (yellow bars) and greater than 2.5 (red bars). Moisture variance budgets were calculated for both (a) SP-CESM and (b) ERAi, where an FMO-like and FMO index was used respectively (see section 2 for details of the indices). The corresponding sample sizes are (a) dark blue = 273, light blue = 489, green = 343, yellow = 159, red = 90 and (b) dark blue = 887, light blue = 1730, green = 1193, yellow = 593, red = 387. The subscripts LP3 and MJO indicate application of 3 day lowpass and 20-100 day bandpass filtering respectively. Please note that term D, the column process, was calculate as the residual of Eulerian moisture tendency and horizontal advection for ERAi (plot (b)).

the increase in horizontal advective damping (Term A) with MJO amplitude results from changes in both horizontal advection by slowly varying fields (Term B) and horizontal advection associated with higher frequency variability (Term C). Figure 21 shows that the net damping effect of higher frequency convective variability (Term A) remains unchanged as MJO amplitude increases, a result of opposing changes in the contributions higher frequency variability makes to large-scale vertical moisture advection (Term B) and horizontal advective damping (Term C).

Terms E and F of Figure 19a show the decomposition of the column process (Term D) into contributions from total radiative heating as well as the net effect of microphysical processes and SGS eddy fluxes respectively. Greater destabilization via radiative heating (Term E) is evident during periods of high MJO amplitude. Figure 22, which shows the decomposition of the slowly varying radiative feedback terms, indicates that the increased destabilization via radiative is primarily the result of intraseasonal variations of longwave radiative heating acting on the background moist thermodynamic profile (Term D) becoming more destabilizing as MJO amplitude increases. Decomposition of this term (not shown) indicates that this increasing strength results from an increase in the strength of intraseasonal variations in longwave heating, not differences in the background moist thermodynamic profile. This is consistent with the findings of *Adames and Kim* [2016], who identified a zonal wavenumber dependence of the cloud-radiative feedback that favored growth at larger scales.

Term F of Figure 19a can be further decomposed into contributions from variations in surface fluxes of moisture (Term G) and SGS convective processes (Term H). Decreased stabilization by surface flux feedbacks
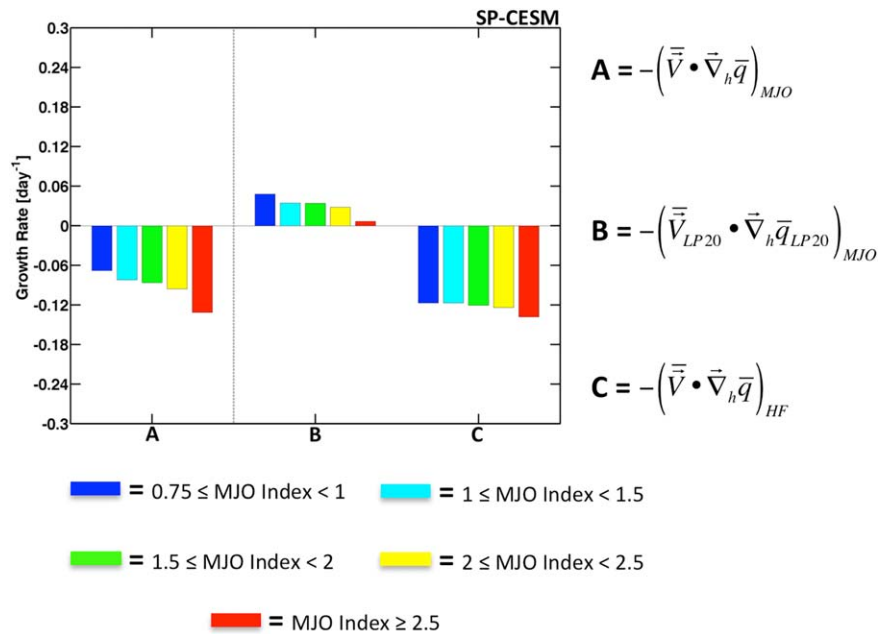
Figure 20. As in Figure 19a, except for various horizontal advective terms. The subscripts LP20 and MJO indicate application of 20 day low-pass and 20-100 day bandpass filtering respectively. The subscript HF indicates terms related to higher frequency variability, calculated following equation (12).

(Term G) is evident during periods of high MJO amplitude. While destabilization by SGS convective processes (Term H) does decrease modestly as MJO amplitude increases, these processes remain a destabilizing force during periods of highest MJO amplitude (red bars).

Figure 23 indicates that the modest decrease in destabilization by SGS convective processes (Term A) is the result of rather dramatic changes in the direct (Term B) and indirect (Term C) effects of SGS convective processes. As MJO amplitude increases, damping by precipitation processes (Term B) increases substantially. This increased damping is almost perfectly opposed by the increased large-scale vertical moisture advection (Term C) driven by intraseasonal variations in heating by SGS convective processes (Term D).
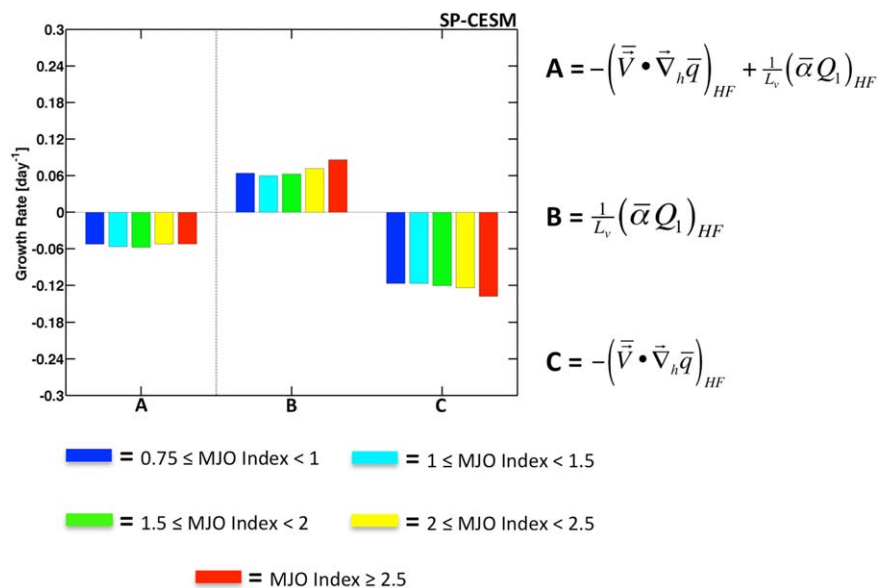

Figure 21. As in Figure 19a, except for terms related to higher frequency convective variability. The subscript HF indicates terms related to higher frequency variability, calculated following equations (12) and (14).
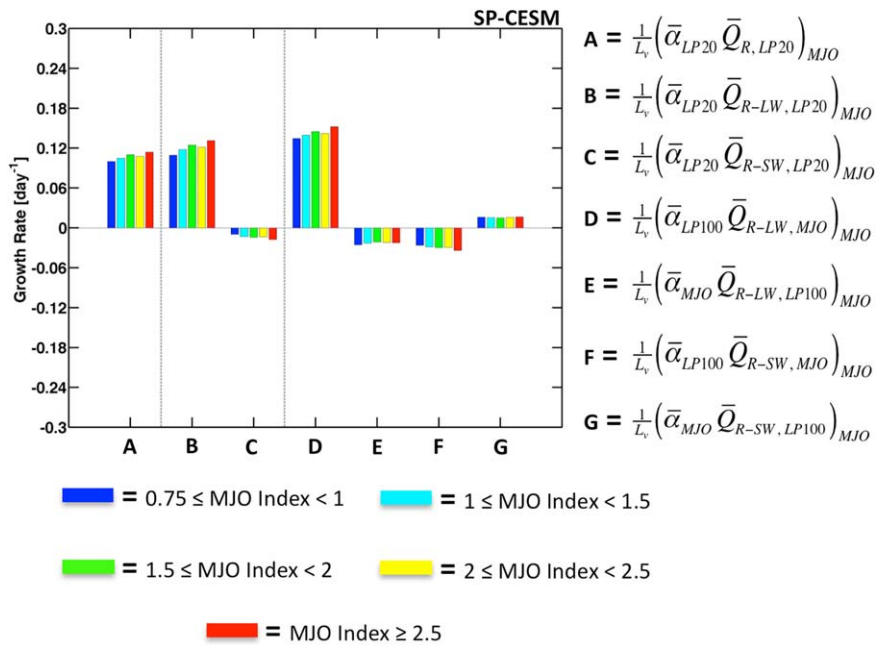
Figure 22. As in Figure 19a, except for various radiative heating terms. Each term was vertically integrated from 850 to 100 hPa, as they depend on the weak temperature gradient approximation. The subscripts LP20, LP100, and MJO indicate application of 20 day lowpass, 100 day lowpass, and 20–100 day bandpass filtering respectively.

Taken together, the results of Figure 19 suggest that changes in the vertical structure of apparent heating (Terms E and H) do not play a dominant role in limiting MJO amplitude, at least in SP-CESM. In other words, the column process does not appear to be strongly "self-limiting" in SP-CESM. While apparent heating may become progressively more top-heavy in regions of enhanced convection as MJO amplitude increases, this appears to play little role in limiting the amplitude of the MJO.

5. Diagnostic Investigation and Interpretation of WTG Balance

Throughout this manuscript, WTG balance has been used as a simplified framework for understanding intra-seasonal variations in large-scale vertical motion. The physical rationale called upon to justify this simplified
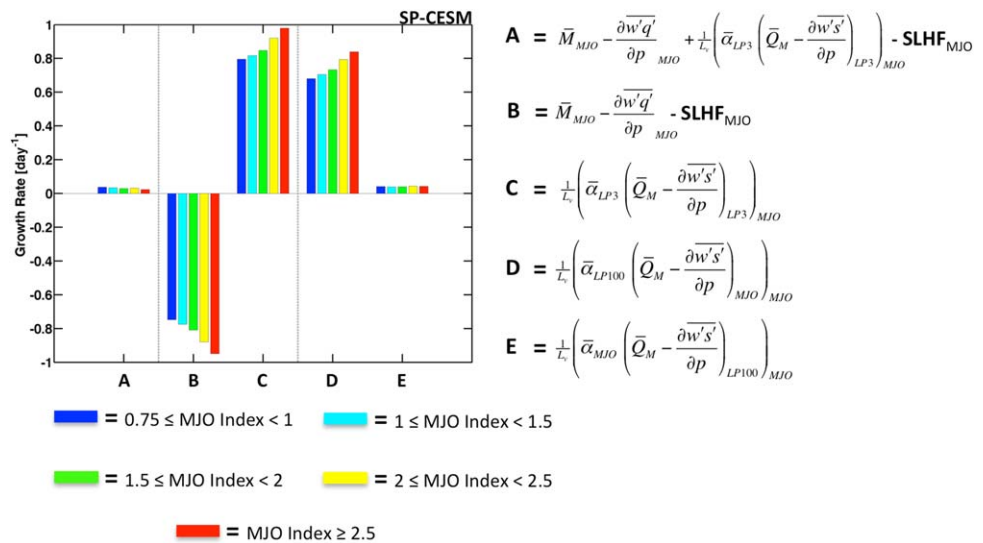

Figure 23. As in Figure 19a, except for various terms relating to subgrid scale convective processes. Each term was vertically integrated from 850 to 100 hPa. The subscripts LP3, LP100, and MJO indicate application of 3 day lowpass, 100 day lowpass, and 20–100 day bandpass filtering respectively.

framework is that of intraseasonal variations in apparent heating undergoing effective gravity wave adjustment, which results in the observed intraseasonal variations in large-scale vertical motion. Demonstrating the ability to accurately diagnose variations in large-scale vertical motion from variations in apparent heating (Figure 6) has been used to legitimize the application of this framework, but does not directly address the physical rationale behind it. That is the aim of this section.

Atmospheric motions occur across a wide range of spatial and temporal scales, and the dynamics that govern such motions vary across this range of scales. Several approaches exist for gaining an understanding of such governing dynamics. Scale analysis is one such approach that has been used with great success, perhaps most notably in understanding midlatitude large-scale dynamics [*Charney*, 1948]. Unfortunately, scale analysis of large-scale tropical dynamics has proven less fruitful, in part because it is "...hard to make relevant equations that are simple, or simple equations that are relevant" [*Vallis*, 2016] for such motions. *Yano and Bonazzola* [2009] highlight that results of scale analyses of large-scale tropical motions [*Charney*, 1963] are "inherently inconclusive" because of considerable sensitivities to small changes in the assumed scales of various terms throughout the analysis. In light of these inherent uncertainties, *Yano and Bonazzola* [2009] employed an alternative approach, whereby the scale dependence of the magnitude of various dynamical terms was estimated using a diagnostic method applied to observational data from the Tropical Ocean and Global Atmosphere (TOGA) Coupled Ocean-Atmosphere Response Experiment (COARE) field campaign. Briefly, this diagnostic method quantified the scale dependence of a variable through application of spatial and temporal moving averages to the TOGA-COARE data. The characteristic magnitude of a variable for a given spatial and temporal scale was estimated by taking the domain average of the root-mean-square of the smoothed variable. The governing dynamics of the given spatial and temporal scale can then be estimated by comparing the characteristic magnitudes of various thermodynamic terms of interest. The reader is referred to *Yano and Bonazzola* [2009, section 7] for further details of this approach.

Here a slightly modified approach is employed, whereby spatial and temporal smoothing is done via wavenumber-frequency filtering instead of application of running means. This modified approach is motivated by knowledge that different governing dynamics may apply to phenomena whose spatial and temporal scales are fairly similar. Here the order of magnitude of a given variable that has been filtered to a specific wavenumber-frequency combination (ω, λ) is estimated using equation (1). Further details of the methodology are provided in section 2.

To assist the assessment and interpretation of WTG balance, three terms of interest are defined as follows

$$\text{W} = \frac{\left[\left(\bar{\omega} \frac{\partial \bar{s}}{\partial p}\right)^2\right]^{\frac{1}{2}}}{\left[(Q_1)^2\right]^{\frac{1}{2}}} (\omega, \lambda) \tag{16}$$

$$\text{T} = \frac{\left[\left(\frac{\partial \bar{s}}{\partial t}\right)^2\right]^{\frac{1}{2}}}{\left[(Q_1)^2\right]^{\frac{1}{2}}} (\omega, \lambda) \tag{17}$$

$$\text{H} = \frac{\left[(\bar{\boldsymbol{V}}_{\boldsymbol{h}} \cdot \nabla \bar{s})^2\right]^{\frac{1}{2}}}{\left[(Q_1)^2\right]^{\frac{1}{2}}} (\omega, \lambda) \tag{18}$$

As discussed earlier, WTG balance refers to a first order balance between large-scale vertical DSE advection and apparent heating in the DSE budget (see equation (3)), where the DSE tendency and horizontal DSE advection are lower order terms. Therefore, the degree to which WTG balance applies can be objectively estimated by looking for regions of wavenumber-frequency space where $0.9 < \text{W} < 1.1$, $\text{T} < 0.1$, and $\text{H} < 0.1$. While these values are chosen to provide some objectivity and clarity in the assessment of the subsequent figure, the reader is encouraged not to consider these as firm thresholds delineating clearly different dynamics, but more as being indicative of dynamical transition regions.

The color shading in Figure 24 shows the thermodynamic balance W for a range of wavenumber-frequency space. First note that the condition $0.9 < \text{W} < 1.1$, which indicates the characteristic magnitude of large-scale
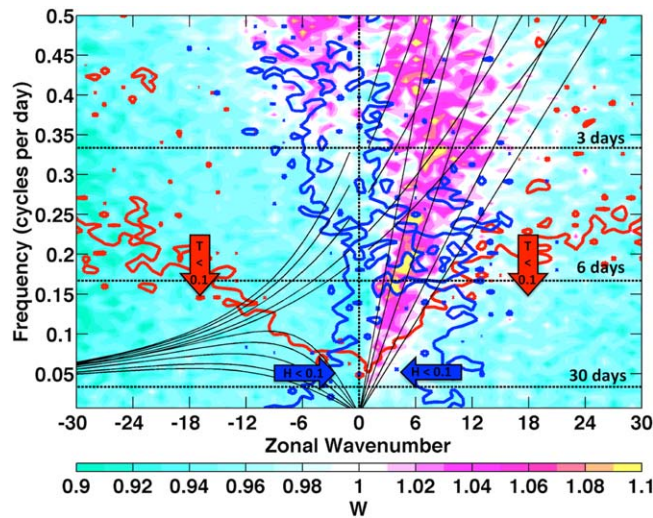
Figure 24. Wavenumber-frequency space of W (shading), the ratio of the characteristic magnitude of large-scale adiabatic cooling to that of apparent heating. Red contours indicate a value of 0.1 for T, the ratio of the characteristic magnitude of the Eulerian dry static energy tendency to that of apparent heating, and red arrows indicate regions where T is less than 0.1. Blue contours indicate a value of 0.1 for H, the ratio of the characteristic magnitude of horizontal dry static energy advection to that of apparent heating, and blue arrows indicate regions where T is less than 0.1. Dispersion curves for equatorial waves of equivalent depths ranging from 8 to 90 m are superimposed in thin black lines. For each term, the characteristic magnitude of the numerator and denominator were calculated separately by filtering each to a single wavenumber-frequency combination. Each term was calculated from fields at 525 hPa. More details of the methodology are provided in section 2.

vertical DSE advection and apparent heating are approximately of the same order, is met nearly everywhere in this space. The value T=0.1 is contoured in red, and red arrows highlight regions where the condition T < 0.1 is met, indicating the characteristic magnitude of DSE tendency is of lower order than that of apparent heating. The value H =0.1 is contoured in blue, and blue arrows highlight regions where the condition H < 0.1 is met, indicating the characteristic magnitude of horizontal DSE advection is of lower order than that of apparent heating. Taken together, these regions indicate that WTG balance is most applicable in a much narrower region of wavenumber-frequency space than would be implied by assessing the thermodynamic balance W alone. This region is characterized by low frequencies and small wavenumbers.

Another interesting feature of Figure 24 is that regions where the thermodynamic balance W exceeds 1 follow dispersion curves (thin black lines) for equatorial Kelvin waves, the eastward component of mixed Rossby gravity (MRG) waves, and the region typically associated with inertio-gravity waves, all strongly divergent phenomena associated with gravity-wave dynamics. As discussed earlier, this paper takes the perspective that intraseasonal variations in large-scale vertical motion are a direct dynamical response to intraseasonal variations in apparent heating, assumed to result from effective gravity wave adjustment occurring on temporal scales much shorter than, and spatial scales much larger than, intraseasonal variations in apparent heating. This perspective portrays local heating as the forcing, the large-scale dynamics as a response, and moisture as the intermediary that couples the two. If this were the case, an upper bound of W=1 may be expected (i.e., large-scale adjustment does not result in adiabatic cooling exceeding apparent heating). But nature is full of examples of large-scale circulations driven, in large part, by processes other than local heating (e.g., midlatitude baroclinic systems), and these large-scale circulations have the ability to force changes in local heating (e.g., through changes in static stability). Such examples may exist in the tropics in the form of certain convectively coupled equatorial waves (CCEW), whose large-scale dry dynamical counterparts do not rely on coupling with diabatic heating, as evidenced by their analytic counterparts originating from simplified sets of equations that contain no representation of such coupling (e.g., the shallow water equations of *Matsuno* [1966]). Findings of several recent studies [*Yasunaga and Mapes*, 2012; *Fuchs et al.*, 2014; *Herman et al.*, 2016] suggest that this perspective, which portrays large-scale dynamics as the forcing and changes in local heating as a response, may apply to strongly divergent CCEWs such as Kelvin waves. Using both observations and idealized modeling, these studies have demonstrated that changes in convective inhibition tend to slightly lead changes in convection in such waves, while changes in moisture tend to lag changes in convection. The finding that W > 1 follows the dispersion curves of strongly divergent CCEWs also supports this perspective. Yet the studies of *Roundy* [2008, 2012], who showed that Kelvin waves can contain considerable rotational components and have OLR power spectra that transition fairly continuously into that of the MJO, suggest that the governing dynamics of Kelvin waves may transition as temporal scales approach those of the MJO. While Figure 24 offers no definitive diagnosis of cause and effect for the relationship of large-scale circulations to apparent heating with the MJO, it is suggestive that the MJO is governed by different dynamics than those of strongly divergent CCEWs, and that WTG balance dynamics are most relevant in a limited region of wavenumber-frequency space where the MJO occurs.

6. Comparison With Previous Studies

This study implements a WTG framework similar to that used in several previous studies, including *Chikira* [2014], *Wolding and Maloney* [2015a], and *Janiga and Zhang* [2016]. Differences in these approaches warrants brief discussion. This study, as well as the studies of *Wolding and Maloney* [2015a] and *Janiga and Zhang* [2016], diagnose the large-scale vertical motion (equation (6)) from the apparent heating. The large-scale vertical motion is the difference between the SGS environmental vertical motion and the cumulus induced SGS environmental vertical motion [*Yanai et al.*, 1973], and represents the effect of large-scale horizontal convergence and divergence acting throughout the column. Using moisture and DSE tendencies resulting from detrainment, *Chikira* [2014] was able to diagnose the SGS environmental vertical motion and cumulus induced SGS environmental vertical motion, in addition to the large-scale vertical motion. While the approach of *Chikira* [2014] is more desirable in that it provides a more detailed picture of the physical processes driving moistening or drying, moisture and DSE tendencies resulting from detrainment are often not known, thereby limiting the applicability of this approach to modeling and observational studies. The benefit of diagnosing the large-scale vertical motion is that is can be done with knowledge of only the apparent heat source and apparent moisture sink (Q_1 and Q_2 respectively), both of which are generally available in modeling and observational studies. In any case, these approaches vary only in the level of detail they provide, not in the physical processes they represent, and therefore the results of the aforementioned studies are directly comparable.

Chikira [2014] analyzed a 10 year simulation of the MJO in the Model for Interdisciplinary Research on Climate (MIROC) version 4.1, which implemented the *Chikira*-Sugiyama cumulus parameterization. *Wolding and Maloney* [2015a] analyzed 34 years of ERAi data, while *Janiga and Zhang* [2016] used the SAM to simulate the November MJO event of the Dynamics of the MJO (DYNAMO) field campaign [*Yoneyama et al.*, 2013; *Johnson and Ciesielski*, 2013]. While the importance of intraseasonal variations in radiative heating was highlighted in each of these studies, they all exhibited vertical profiles of radiative heating anomalies that appear to be considerably more "top-heavy" than those observed in this study. The relatively bottom-heavy profiles of radiative heating anomalies in SP-CESM, which will drive relatively large moisture tendencies because of the large value of $\bar{\alpha}$ at low levels, may contribute to the apparent excessive instability of the column process noted earlier (Figures. 10a and 11a). Figures 7d and 10b support the findings of *Wolding and Maloney* [2015a] and *Janiga and Zhang* [2016], who noted the importance of low level heating and SGS eddy fluxes in moistening low and mid levels during the transition from suppressed to enhanced convection. During the enhanced phase, *Janiga and Zhang* [2016] emphasize the role of SGS eddy fluxes in maintaining midlevel moisture, while *Chikira* [2014] finds that radiative heating anomalies play a dominant role. While the results of this study (Figure 9a) are, at first glance, more supportive of the findings of *Janiga and Zhang* [2016], we interpret this as being the vertical redistribution of moisture provided at low levels by the radiative driven anomalous convergence.

A secondary goal of this study was to compare and contrast the WTG balance framework with more traditional column MSE budget analyses of the MJO. While numerous previous studies have used the column MSE budget to investigate the MJO [*Maloney*, 2009; *Maloney et al.*, 2010; *Kiranmayi and Maloney*, 2011; *Andersen and Kuang*, 2012; *Wu and Deng*, 2013; *Kim et al.*, 2014a; *Sobel et al.*, 2014; *Arnold et al.*, 2015], this discussion will focus on the results of *Arnold et al.* [2015], who analyzed the same simulation used in this study. Figures 10 and 12 in *Arnold et al.* [2015] can be compared to Figures 10a,b from this study for reference during the following discussion. Using a column MSE variance budget, *Arnold et al.* [2015] concluded that the MJO was a radiative driven instability damped by horizontal advection, largely consistent with the findings of previous sections. Direct comparison of assessments made using the column MSE and WTG balance frameworks shows that, in most cases, both frameworks come to very similar conclusions regarding the contributions that individual processes (e.g., longwave radiative heating and SLHF) make to the growth and propagation of moisture/MSE anomalies. Yet these two frameworks come to opposite conclusions regarding the role of variations in SW radiative heating, which the column MSE framework deems to be a destabilizing process [*Arnold et al.*, 2015, Figure 10], and which the WTG framework deems to be a stabilizing process (Figure 17b).

Inspection of Figures 17e and 17f provides some insight as to why these two approaches differ, and highlights the importance of quantitatively partitioning the vertical advection term of the MSE budget. During

the enhanced phase, anomalous SW radiative heating in the upper troposphere exceeds anomalous SW cooling in the lower troposphere, such that the column integrated effect (not shown) is a net heating. As this is associated with a positive MSE tendency, this net heating appears as to act as a positive feedback [see *Arnold et al.*, 2015, Figure 10] when assessed using a column MSE approach. Yet Figure 17f highlights that, because of the high moisture sensitivity of the lower troposphere, the anomalous SW radiative cooling at low and mid levels produces considerable drying, and results in a net drying of the column. This net drying of the column, which gets lumped into the vertical advection term of the MSE budget, is a negative feedback and is accurately assessed using the WTG balance framework (Figure 17b). The results of *Muller and Held* [2012], who found that interactive SW radiation opposed aggregation, support the conclusion that variations in SW radiative heating act as a negative feedback for the MJO.

The differing assessments of the SW radiative feedback underscore a fundamental distinction that must be made between column integrated MSE and column integrated moisture, which are sometimes given a false equivalence on intraseasonal timescales. While it is true that, under WTG balance, column MSE anomalies are approximately equal to column moisture anomalies, processes that drive changes in MSE do not necessarily drive equivalent changes in moisture, as evidenced by variations in SW radiative heating. In the case of SW radiative heating, the column MSE framework measures its direct effect on column DSE, while its effect on moisture (by driving large-scale vertical moisture advection) ends up lumped in with the vertical MSE advection term. This distinction can be the source of misinterpretation of results based on the column MSE framework, and metrics derived from column MSE (e.g., gross moist stability), if such tools do not evoke a clear and tangible connection to the physical processes at work in the minds of their users. The authors of this study believe that the WTG balance framework provides a more accurate and easily understood assessment of the relationship between heating, large-scale vertical motion, and moisture.

7. Conclusions

The superparameterized Community Earth System Model (SP-CESM) was used to investigate the MJO, with a primary focus on understanding the relationship between moisture, apparent heating, and large-scale vertical motion. In this study, the MJO is viewed as a slowly moving *Matsuno*-Gill pattern maintained by positive feedbacks between moisture, apparent heating, and large-scale dynamics. Intraseasonal variations in large-scale vertical motion are viewed as the result of effective gravity wave adjustment of intraseasonal variations in apparent heating. This dynamical response alters the large-scale distribution of moisture which, through convective scale processes such as entrainment, influences subsequent apparent heating and results in the aforementioned positive feedback. This perspective of the MJO is outlined in Figure 4.

WTG theory provides a useful framework for understanding the relationship between moisture, apparent heating, and large-scale vertical motion, allowing intraseasonal variations in large-scale vertical motion to be accurately diagnosed from apparent heating. Large-scale vertical moisture advection can therefore be decomposed into contributions from various apparent heating processes, including microphysical processes, SGS eddy fluxes, and radiative heating. In this study, the WTG framework has been used to arrive at the following main conclusions:

1. the MJO is strongly supported by radiative feedbacks and damped by horizontal advection, consistent with the findings of previous studies
2. higher frequency convective variability contributes to damping by horizontal advection as well as destabilization by large-scale vertical moisture advection
3. the evolution of the vertical structure of apparent heating does not play a dominant role in limiting the strength of MJO convection in SP-CESM

Each of these conclusions will now be discussed in turn.

While results from SP-CESM moisture and moisture variance budgets clearly support the conclusion that the MJO is strongly supported by radiative feedbacks, they suggest that such feedbacks may not be essential to the MJO, at least in SP-CESM. This is consistent with the findings of *Arnold and Randall* [2015], who showed that MJO-like activity persisted in a rotating global aqua-planet SP-CESM simulation when longwave radiative feedbacks were removed. Comparison of SP-CESM and ERAi moisture variance budgets suggests the former may have an unrealistically unstable column process, likely a result of excessive

destabilization by radiative feedbacks or SGS convective processes. Discussion provided below may offer more insight to this issue.

Destabilization of the MJO is primarily limited by horizontal advective damping, which is accomplished through the modulation of higher frequency convective variability [*Maloney and Dickinson*, 2003; *Maloney*, 2009; *Maloney et al.*, 2010; *Kiranmayi and Maloney*, 2011; *Andersen and Kuang*, 2012; *Chikira*, 2014]. This study has shown that the modulation of higher frequency convective variability also enhances anomalous large-scale vertical moisture advection, which helps to destabilize the MJO. While the net effect of higher frequency convective variability remains a damping one, higher frequency variability may not play as important a role in limiting the strength of the MJO as once perceived by considering its horizontal advective damping effects alone.

Moisture variance budgets were used to assess how the strength of various feedbacks change as MJO amplitude increases. It was found that destabilization by radiative feedbacks actually increased as MJO amplitude increased. Perhaps more interesting is that the destabilizing effect of SGS convective processes showed only a modest decrease as MJO amplitude increased, and remained a destabilizing force even during periods of highest MJO amplitude. This occurs despite a dramatic increase in the damping effect of precipitation, and results from the near perfect compensation by large-scale vertical moisture advection driven by convective heating. To state this another way, heating released by increased precipitation drives enough large-scale vertical moisture advection to replace the moisture directly removed by increased precipitation, or $\Delta\langle\bar{\alpha}(Q_1-\bar{Q}_R)\rangle \approx \Delta\langle\langle(Q_1-\bar{Q}_R)\rangle\rangle$, where Δ is change associated with a change in MJO amplitude. Taken together with the increasing strength of the radiative feedback, this leads to the conclusion that changes in the vertical structure of apparent heating structure play little role in limiting MJO amplitude, at least in SP-CESM. This is important because it implies that MJO amplitude ceases to increase when horizontal advective damping has become sufficiently strong, not when destabilization by the column process has become sufficiently weak. While apparent heating may become progressively more top-heavy in regions of enhanced convection as MJO amplitude increases, this appears to play little role in limiting the amplitude of the MJO. Destabilization by the column process does not appear to be strongly "self-limiting."

But how is it that, as MJO convective anomalies increase in magnitude, and the convective heating profile becomes progressively more top-heavy, heating can continue to drive sufficient large-scale vertical moisture advection to result in destabilization? Inspection of Figure 5a, which shows the moisture sensitivity to apparent heating, offers a suggestion. The large moisture sensitivity of the lower troposphere means that a small increase in heating at lower levels can drive comparably large amounts of large-scale vertical moisture advection. Therefore, as long as sufficient increases in low level heating occur coincidentally with increased heating at upper levels, the heating profile may become progressively more top heavy but still drive sufficient large-scale vertical moisture advection to remain unstable. This idea is consistent with the findings of *Riley et al.* [2011], who used CloudSat observations to show that increased occurrence of all cloud types occur during the enhanced phase of the MJO. This idea would also suggest that convective schemes lacking the ability to simulate the coincidental enhancement of both shallow and deep convection may have difficulties simulating instabilities driven by SGS convective processes.

The findings of this study suggest the following physical picture of the MJO in SP-CESM. The enhanced phase of the MJO is characterized by a considerable increase in convective activity over a large geographic region. Phrases such as "convective moistening" are often used to describe convective processes occurring on the SGS (i.e., microphysical processes and SGS eddy fluxes). While these processes can act to moisten the atmosphere at certain levels by vertically redistributing moisture throughout the column, this vertical redistribution often comes at a cost to column moisture, which is removed by precipitation processes. The net effect is such that, during the enhanced phase when precipitation increases, convective processes occurring on the SGS act to warm and dry the column on the large-scale. When such processes occur over several days or more in the tropics, very little of the aforementioned warming is realized, as effective gravity wave adjustment results in low level mass convergence, large-scale ascent, and adiabatic cooling that balances the warming. This low level mass convergence represents the drawing in of moist air from distant regions, which is returned at upper levels in a much drier condition. During the enhanced phase, the increased large-scale convergence resulting from warming by SGS convective processes alone (i.e., without variations in radiative heating) brings with it more than enough moisture to offset the increased drying by SGS convective processes. The enhanced phase is also accompanied by a reduction in longwave radiative

cooling, which drives additional low level moisture convergence. The result is that the enhancement of convection over a large geographic region converges more moisture than it removes via precipitation, allowing enhanced precipitation to be sustained (or even amplified), despite reduced surface fluxes of moisture, which are suppressed in the enhanced phase of the MJO in SP-CESM. The ability of convection to acquire moisture from remote sources is what permits the coexistence of minima in surface fluxes of moisture and maxima in precipitation observed over the warm pool [*Sobel*, 2003]. A similar coexistence of minima in surface fluxes of moisture and maxima in precipitation is observed during the enhanced phase of the MJO in SP-CESM, suggesting that understanding the mechanisms whereby convection acquires moisture from remote sources is crucial to understanding the moisture-convection feedback thought to drive the MJO.

Examination of Figure 4 highlights the numerous difficulties faced when trying to understand and simulate the MJO. First note the incredible range of scales encompassed by the processes that appear to be crucial to the MJO, which span from small scale processes such as entrainment and microphysics to the global scale dynamical response. While GCMs are able to span the global scale dynamical response, many do not exhibit an appropriate sensitivity of convection to free tropospheric humidity [*Thayer-Calder and Randall*, 2009], emblematic of the poor representation of small scale processes (bottom left arrows) such as entrainment [*Hannah and Maloney*, 2014]. Yet CSRMs, while able to represent small scale process more realistically, are often computationally limited to domains which only encompass a fraction of the large-scale dynamical response. Only recent generations of models have begun to effectively span the range of scales necessary to produce realistic intraseasonal variability [*Randall et al.*, 2003; *Raymond and Zeng*, 2005; *Sessions et al.*, 2010; *Bretherton and Khairoutdinov*, 2015; *Arnold and Randall*, 2015]. Even when a model is able to realistically represent processes across this range of scales, a model's climate may produce unrealistic feedbacks between these various processes. The dynamical response to apparent heating (top arrow) will be scaled by a model's static stability, while the resulting moisture convergence (bottom right arrow) will be closely related to a model's $\bar{\alpha}$. Such factors may help to explain not only why some models produce insufficient intraseasonal variability, but also why some models produce intraseasonal variability with characteristics different from that of the real world.

Phenomena are often distinguished by their organizing forces, a custom borne more from understanding than from the desire to categorize. Advancing understanding of both the MJO and convective aggregation may be accelerated by continuing to seek out and apply meaningful process oriented diagnostics to these phenomena. Given the weak destabilizing effect of convection alone (i.e., in the absence of radiative and surface flux feedbacks), it seems reasonable to expect that a positive feedback between moisture, heating, and large-scale dynamics could be achieved through a different combination of processes than those that occur in SP-CESM. Process oriented diagnostics should assess not only if a model is simulating sufficiently strong feedbacks between moisture, heating, and large-scale dynamics, but also that such feedbacks are driven by the "correct" combination of stabilizing and destabilizing processes. Successful implementation of such diagnostics will require the "correct" combination of stabilizing and destabilizing processes of the real world MJO be better constrained. In particular, more work must be done to constrain the vertical profile of radiative heating [*Lin et al.*, 2004; *Ma and Kuang*, 2011; *Jiang et al.*, 2011], and how this profile relates to destabilization by the column process.

References

Adames, Á. F., and D. Kim (2016), The mjo as a dispersive, convectively coupled moisture wave: Theory and observations, *J. Atmos. Sci.*, *73*, 913–941.

Andersen, J. A., and Z. Kuang (2012), Moist static energy budget of MJO-like disturbances in the atmosphere of a zonally symmetric aquaplanet, *J. Clim.*, *25*(8), 2782–2804.

Arnold, N. P., and D. A. Randall (2015), Global-scale convective aggregation: Implications for the Madden-Julian oscillation, *J. Adv. Model. Earth Syst.*, *7*, 1499–1518, doi:10.1002/2015MS000498.

Arnold, N. P., M. Branson, Z. Kuang, D. A. Randall, and E. Tziperman (2015), MJO intensification with warming in the superparameterized CESM, *J. Clim.*, *28*(7), 2706–2724.

Benedict, J. J., and D. A. Randall (2007), Observed characteristics of the MJO relative to maximum rainfall, *J. Atmos. Sci.*, *64*(7), 2332–2354.

Benedict, J. J., and D. A. Randall (2009), Structure of the Madden-Julian oscillation in the superparameterized CAM, *J. Atmos. Sci.*, *66*(11), 3277–3296.

Bony, S., et al. (2015), Clouds, circulation and climate sensitivity, *Nat. Geosci.*, *8*(4), 261–268.

Bretherton, C. S., and M. F. Khairoutdinov (2015), Convective self-aggregation feedbacks in near-global cloud-resolving simulations of an aquaplanet, *J. Adv. Model. Earth Syst.*, *7*, 1765–1787, doi:10.1002/2015MS000499.

Bretherton, C. S., P. N. Blossey, and M. Khairoutdinov (2005), An energy-balance analysis of deep convective self-aggregation above uniform SST, *J. Atmos. Sci.*, *62*(12), 4273–4292.

Charney, J. (1948), On the scale of atmospheric motions, *Geofys. Publikasjoner*, *17*, 1–17.

Charney, J. G. (1963), A note on large-scale motions in the tropics, *J. Atmos. Sci.*, *20*(6), 607–609.

Chikira, M. (2014), Eastward-propagating intraseasonal oscillation represented by Chikira–Sugiyama cumulus parameterization. part ii: Understanding moisture variation under weak temperature gradient balance, *J. Atmos. Sci.*, *71*(2), 615–639, doi:10.1175/JAS-D-13-038.1.

Dee, D., et al. (2011), The ERA-interim reanalysis: Configuration and performance of the data assimilation system, *Q. J. R. Meteorol. Soc.*, *137*(656), 553–597.

Fuchs, Z., and D. J. Raymond (2005), Large-scale modes in a rotating atmosphere with radiative-convective instability and wishe, *J. Atmos. Sci.*, *62*(11), 4084–4094.

Fuchs, Ž., S. L. Sessions, and D. J. Raymond (2014), Mechanisms controlling the onset of simulated convectively coupled kelvin waves, *Tellus, Ser. A*, *66*, 1–8.

Grabowski, W. W. (2001), Coupling cloud processes with the large-scale dynamics using the cloud-resolving convection parameterization (CRCP), *J. Atmos. Sci.*, *58*(9), 978–997.

Grabowski, W. W. (2004), An improved framework for superparameterization, *J. Atmos. Sci.*, *61*(15), 1940–1952.

Grabowski, W. W., and M. Moncrieff (2004), Moisture–convection feedback in the tropics, *Q. J. R. Meteorol. Soc.*, *130*(604), 3081–3104.

Hannah, W. M., and E. D. Maloney (2014), The moist static energy budget in NCAR cam5 hindcasts during dynamo, *J. Adv. Model. Earth Syst.*, *6*, 420–440, doi:10.1002/2013MS000272.

Herman, M. J., Z. Fuchs, D. J. Raymond, and P. Bechtold (2016), Convectively coupled kelvin waves: From linear theory to global models, *J. Atmos. Sci.*, *73*(1), 407–428.

Hurrell, J. W., et al. (2013), The community earth system model: A framework for collaborative research, *Bull. Am. Meteorol. Soc.*, *94*(9), 1339–1360.

Janiga, M. A., and C. Zhang (2016), MJO moisture budget during dynamo in *a cloud-resolving model, J. Atmos. Sci.*, 2257–2278.

Jiang, X., D. E. Waliser, W. S. Olson, W.-K. Tao, T. S. L'Ecuyer, K.-F. Li, Y. L. Yung, S. Shige, S. Lang, and Y. N. Takayabu (2011), Vertical diabatic heating structure of the MJO: Intercomparison between recent reanalyses and TRMM estimates, *Mon. Weather Rev.*, *139*(10), 3208–3223.

Johnson, R., and P. Ciesielski (2013), Structure and properties of Madden-Julian Oscillations deduced from DYNAMO sounding arrays, *J. Atmos. Sci.*, *70*, 3157–3179.

Khairoutdinov, M. F., and D. A. Randall (2003), Cloud resolving modeling of the arm summer 1997 IOP: Model formulation, results, uncertainties, and sensitivities, *J. Atmos. Sci.*, *60*(4), 607–625.

Kiladis, G. N., J. Dias, K. H. Straub, M. C. Wheeler, S. N. Tulich, K. Kikuchi, K. M. Weickmann, and M. J. Ventrice (2014), A comparison of OLR and circulation-based indices for tracking the MJO, *Mon. Weather Rev.*, *142*(5), 1697–1715.

Kim, D., A. H. Sobel, and I.-S. Kang (2011), A mechanism denial study on the Madden-Julian Oscillation, *J. Adv. Model. Earth Syst.*, *3*, M12007, doi:10.1029/2011MS000081.

Kim, D., J.-S. Kug, and A. H. Sobel (2014a), Propagating versus nonpropagating Madden–Julian Oscillation events, *J. Clim.*, *27*(1), 111–125.

Kim, D., M.-I. Lee, D. Kim, S. D. Schubert, D. E. Waliser, and B. Tian (2014b), Representation of tropical subseasonal variability of precipitation in global reanalyses, *Clim. Dyn.*, *43*(1-2), 517–534.

Kiranmayi, L., and E. D. Maloney (2011), Intraseasonal moist static energy budget in reanalysis data, *J. Geophys. Res.*, *116*, D21117, doi:10.1029/2011JD016031.

Lau, K., and H. Wu (2010), Characteristics of precipitation, cloud, and latent heating associated with the Madden-Julian Oscillation, *J. Clim.*, *23*(3), 504–518.

Lin, J., B. Mapes, M. Zhang, and M. Newman (2004), Stratiform precipitation, vertical heating profiles, and the Madden-Julian Oscillation, *J. Atmos. Sci.*, *61*(3), 296–309.

Lin, J.-L., et al. (2006), Tropical intraseasonal variability in 14 IPCC ar4 climate models. part i: Convective signals, *J. Clim.*, *19*(12), 2665–2690.

Lucas, C., E. J. Zipser, and M. A. Lemone (1994), Vertical velocity in oceanic convection off tropical Australia, *J. Atmos. Sci.*, *51*(21), 3183–3193.

Ma, D., and Z. Kuang (2011), Modulation of radiative heating by the Madden-Julian Oscillation and convectively coupled Kelvin waves as observed by CloudSat, *Geophys. Res. Lett.*, *38*, L21813, doi:10.1029/2011GL049734.

Maloney, E. D. (2009), The moist static energy budget of a composite tropical intraseasonal oscillation in a climate model, *J. Clim.*, *22*(3), 711–729.

Maloney, E. D., and M. J. Dickinson (2003), The intraseasonal oscillation and the energetics of summertime tropical western north pacific synoptic-scale disturbances, *J. Atmos. Sci.*, *60*(17), 2153–2168.

Maloney, E. D., A. H. Sobel, and W. M. Hannah (2010), Intraseasonal variability in an aquaplanet general circulation model, *J. Adv. Model. Earth Syst.*, *2*, 5, doi:10.3894/JAMES.2010.2.

Matsuno, T. (1966), Quasi-geostrophic motions in the equatorial area, *J. Meteorol. Soc. Jpn.*, *44*(1), 25–43.

Morita, J., Y. N. Takayabu, S. Shige, and Y. Kodama (2006), Analysis of rainfall characteristics of the Madden–Julian Oscillation using TRMM satellite data, *Dyn. Atmos. Oceans*, *42*(1), 107–126.

Muller, C., and S. Bony (2015), What favors convective aggregation and why?, *Geophys. Res. Lett.*, *42*, 5626–5634, doi:10.1002/2015GL064260.

Muller, C. J., and I. M. Held (2012), Detailed investigation of the self-aggregation of convection in cloud-resolving simulations, *J. Atmos. Sci.*, *69*(8), 2551–2565.

North, G. R., T. L. Bell, R. F. Cahalan, and F. J. Moeng (1982), Sampling errors in the estimation of empirical orthogonal functions, *Mon. Weather Rev.*, *110*(7), 699–706.

Randall, D., M. Khairoutdinov, A. Arakawa, and W. Grabowski (2003), Breaking the cloud parameterization deadlock, *Bull. Am. Meteorol. Soc.*, *84*(11), 1547–1564.

Raymond, D. J. (2001), A new model of the Madden-Julian Oscillation, *J. Atmos. Sci.*, *58*(18), 2807–2819.

Raymond, D. J., and Ž. Fuchs (2009), Moisture modes and the madden-julian oscillation, *J. Clim.*, *22*(11), 3031–3046.

Raymond, D. J., and X. Zeng (2005), Modelling tropical atmospheric convection in the context of the weak temperature gradient approximation, *Q. J. R. Meteorol. Soc.*, *131*(608), 1301–1320.

Riley Dellaripa, E. M., and E. D. Maloney (2015), Analysis of MJO wind-flux feedbacks in the Indian ocean using RAMA buoy observations, *J. Meteorol. Soc. Jpn.*, *2*, *93*, 1–20.

Riley, E. M., B. E. Mapes, and S. N. Tulich (2011), Clouds associated with the Madden-Julian Oscillation: A new perspective from cloudsat, *J. Atmos. Sci.*, *68*(12), 3032–3051.

Roundy, P. E. (2008), Analysis of convectively coupled Kelvin waves in the Indian ocean MJO, *J. Atmos. Sci.*, *65*(4), 1342–1359.

Roundy, P. E. (2012), Tracking and prediction of large-scale organized tropical convection by spectrally focused two-step space–time eof analysis, *Q. J. R. Meteorol. Soc.*, *138*(665), 919–931.

Sahany, S., J. D. Neelin, K. Hales, and R. B. Neale (2012), Temperature-moisture dependence of the deep convective transition as a constraint on entrainment in climate models, *J. Atmos. Sci.*, *69*(4), 1340–1358.

Sessions, S. L., S. Sugaya, D. J. Raymond, and A. H. Sobel (2010), Multiple equilibria in a cloud-resolving model using the weak temperature gradient approximation, *J. Geophys. Res.*, *115*, D12110, doi:10.1029/2009JD013376.

Sherwood, S. C. (1999), On moistening of the tropical troposphere by cirrus clouds, *J. Geophys. Res.*, *104*, 11,949–11,960.

Sobel, A., and E. Maloney (2012), An idealized semi-empirical framework for modeling the MaJden-Julian Oscillation, *J. Atmos. Sci.*, *69*(5), 1691–1705.

Sobel, A., S. Wang, and D. Kim (2014), Moist static energy budget of the MJO during dynamo, *J. Atmos. Sci.*, *71*(11), 4276–4291, doi:10.1175/JAS-D-14-0052.1.

Sobel, A. H. (2003), On the coexistence of an evaporation minimum and precipitation maximum in the warm pool, *J Clim.*, *16*(6), 1003–1009.

Sobel, A. H., J. Nilsson, and L. M. Polvani (2001), The weak temperature gradient approximation and balanced tropical moisture waves*, *J. Atmos. Sci.*, *58*, 3650–3665.

Stan, C., M. Khairoutdinov, C. A. DeMott, V. Krishnamurthy, D. M. Straus, D. A. Randall, J. L. Kinter, and J. Shukla (2010), An ocean-atmosphere climate simulation with an embedded cloud resolving model, *Geophys. Res. Lett.*, *37*, L01702, doi:10.1029/2009GL040822.

Stocker, T., D. Qin, G.-K. Plattner, M. Tignor, S. K. Allen, J. Boschung, A. Nauels, Y. Xia, V. Bex, and P. M. Midgley (2014), *Climate change 2013: The Physical Science Basis*, Cambridge Univ. Press Cambridge, U. K.

Thayer-Calder, K., and D. A. Randall (2009), The role of convective moistening in the madden-julian oscillation, *J. Atmos. Sci.*, *66*(11), 3297–3312.

Tian, B., D. E. Waliser, E. J. Fetzer, and Y. L. Yung (2010), Vertical moist thermodynamic structure of the Madden-Julian Oscillation in atmospheric infrared sounder retrievals: An update and a comparison to ecmwf interim re-analysis, *Mon. Weather Rev.*, *138*(12), 4576–4582.

Tompkins, A. M. (2001), Organization of tropical convection in low vertical wind shears: The role of water vapor, *J. Atmos. Sci.*, *58*(6), 529–545.

Vallis, G. K. (2016), *Atmospheric and Oceanic Fluid Dynamics: Fundamentals and Large-Scale Circulation*, 2nd ed., Cambridge Univ. Press, Cambridge, U. K.

Wheeler, M., and G. N. Kiladis (1999), Convectively coupled equatorial waves: Analysis of clouds and temperature in the wavenumber–frequency domain, *J. Atmos. Sci.*, *56*(3), 374–399, doi:10.1175/1520-0469(1999)056¡0374:CCEWAO¿2.0.CO;2.

Wheeler, M. C., and H. H. Hendon (2004), An all-season real-time multivariate MJO index: Development of an index for monitoring and prediction, *Mon. Weather Rev.*, *132*(8), 1917–1932.

Wing, A. A., and K. A. Emanuel (2014), Physical mechanisms controlling self-aggregation of convection in idealized numerical modeling simulations, *J. Adv. Model. Earth Syst.*, *6*, 59–74.

Wolding, B. O., and E. D. Maloney (2015a), Objective diagnostics and the madden–julian oscillation. part ii: Application to moist static energy and moisture budgets, *J. Clim.*, *28*(19), 7786–7808.

Wolding, B. O., and E. D. Maloney (2015b), Objective diagnostics and the madden-julian oscillation. part i: Methodology, *J. Clim.*, *28*, 7786–7808, doi:10.1175/JCLI-D-14-00688.1.

Wu, X., and L. Deng (2013), Comparison of moist static energy and budget between the gcm-simulated madden-julian oscillation and observations over the Indian Ocean and western pacific, *J. Clim.*, *26*(14), 4981–4993.

Yanai, M., and R. Johnson (1993), Impacts of cumulus convection on thermodynamic fields, *Meteorol. Monogr.*, *24*, 39–62.

Yanai, M., S. Esbensen, and J.-H. Chu (1973), Determination of bulk properties of tropical cloud clusters from large-scale heat and moisture budgets, *J. Atmos. Sci.*, *30*(4), 611–627.

Yano, J.-I., and M. Bonazzola (2009), Scale analysis for large-scale tropical atmospheric dynamics, *J. Atmos. Sci.*, *66*(1), 159–172.

Yasunaga, K., and B. Mapes (2012), Differences between more divergent and more rotational types of convectively coupled equatorial waves. Part i: Space-time spectral analyses, *J. Atmos. Sci.*, *69*(1), 3–16.

Yoneyama, K., C. Zhang, and C. N. Long (2013), Tracking pulses of the Madden-Julian oscillation, *Bull. Am. Meteorol. Soc.*, *94*(12).

Zipser, E. J. (2003), Some views on "hot towers" after 50 years of tropical field programs and two years of TRMM data, *Meteorol. Monogr.*, *29*(51), 49–58.